

# Post-process correction improves the accuracy of satellite PM<sub>2.5</sub> retrievals - Authors response

Andrea Porcheddu, Ville Kolehmainen, Timo Lähivaara, Antti Lipponen

We would like to thank the reviewers for reading carefully the manuscript and giving their comments. Here below we report the changes we have made to the manuscript. In the following pages the questions from the reviewers and the related answers from the authors can be found. At the end of the document we report a version of the manuscript realized with latexdiff in order to show explicitly the changes.

## 5 1 Changes made following reviewer #1 questions

- Temporal resolution and swath of the sensor (for what regards satellite data) have been added to the manuscript in Section 2.1.
- Longitude and latitude have been added to the panels in fig.5 and 6.
- The method cited in section 2.2 has been explained in more details.
- 10 – The unit of RMSE and other missing units have been added to the manuscript.

## 2 Changes made following reviewer #2 questions

- The abstract has been extended.
- The introduction has been extended.
- We added the resolution for OpenStreetMap roads data and NASA Black Marble Night Lights data in section 2.6.1 and 15 2.6.2, respectively.
- We modified table A1 reporting now the features in order of feature importance (where the feature importance come from a SHAP analysis). We also added a barplot in fig.A1 where all the first 26 features by feature importance are represented. We extended Section 3.3 at line 208-212 explaining how we used SHAP analysis and what conclusions we made.

## 3 Changes made following questions by Adam Povey, Supriya Mantri, and Laura Horton

- 20 – At line 116, an explanation to the RH equation has been added.

- We included a reference to the NASA Black Marble Night Lights dataset used in section 2.6.2.
- We added two equations in section 3.3 to better explain how the post-process correction is applied to estimate  $PM_{2.5}$  levels.
- Fig.3 has been modified to improve its readability (and a label for the y axis has been added).
- 25 – The top-right panels in fig.5 and 6 now present a green arrow with green larger text in order to improve readability.
- Various typographic errors have been corrected.

#### 4 More

- Based on comment 2.6 (below) on possible correlations due to the monitoring stations proximity, we are now considering only the closest pixel to each Open AQ monitoring station instead of all the pixels available within a certain radius. Based  
30 on comment 1.5 (below) on the monthly averages, we modified the calculation of monthly averages so that monthly averages are calculated when satellite data is available for 5 or more days. These changes in the data processing induced minor changes in the overall error metrics in Figs. 4, 5, 6, and 7, but they did not affect the findings or conclusions of the manuscript.

# Post-process correction improves the accuracy of satellite PM<sub>2.5</sub> retrievals - Reply to referees

Andrea Porcheddu, Ville Kolehmainen, Timo Lähivaara, Antti Lipponen

We would like to thank the reviewers for reading carefully the manuscript and giving their comments. Below we reply to each of the comments.

## 1 Answers to reviewer #1

**1.1 There are many researches that focus on using AOD to estimate PM<sub>2.5</sub> through machine learning approaches.**

5 **Compared with them, what is the innovation of this study? I understand that this study corrects the ratio between PM<sub>2.5</sub> and AOD derived from MERRA2 and applies the improved ratio to satellite AOD to estimate surface PM<sub>2.5</sub> concentrations, which is different from other researches that estimate PM<sub>2.5</sub> directly. Although this is a new approach, what is the advantage of this study. Compared with previous researches, can the new approach provide better PM<sub>2.5</sub> estimation?**

10 The novelty of this study is to employ the post process correction where we use machine learning for correcting the geophysical model based AOD-to-PM<sub>2.5</sub> conversion ratio instead of directly predicting the conversion ratio. The rationale for this selection is improved accuracy over the conventional approach of learning the conversion ratio directly. Figure 1 shows the results obtained with the conventional approach of learning directly the AOD-to-PM<sub>2.5</sub> ratio. The  $R^2$ , RMSE and MAE with the proposed post-correction approach (left image) are better than with the conventional direct estimation (right image).

15 **1.2 This exclude the PM<sub>2.5</sub> concentrations that are larger than 80  $\mu\text{g}/\text{m}^3$ . This would reduce the importance of this study as the research community is more interested in heavy polluted scene. The authors excluded that condition that PM<sub>2.5</sub> concentrations that are larger than 80  $\mu\text{g}/\text{m}^3$  due to imbalanced data (only a small set of data with PM<sub>2.5</sub> concentrations that are larger than 80  $\mu\text{g}/\text{m}^3$ ). Can the problem is solved through bagging or other approaches?**

20 The PM<sub>2.5</sub> values beyond 80  $\mu\text{g}/\text{m}^3$  were excluded from the study due to sparsity of high value data in the region of interest (central Europe, 2019) considered in this study. Similar cutoff for high PM<sub>2.5</sub> values has been applied, for example, in Ibrahim et al. (2022)). To address the lack of high PM<sub>2.5</sub> data, one could think of producing synthetic training data using machine learning models such as TVAE (Tabular Variational Auto Encoder) or CTGAN (Conditional Tabular Generative Adversarial Network) (Xu et al., 2019): we tried already to use them to balance the data but they did not improve the results. In future studies

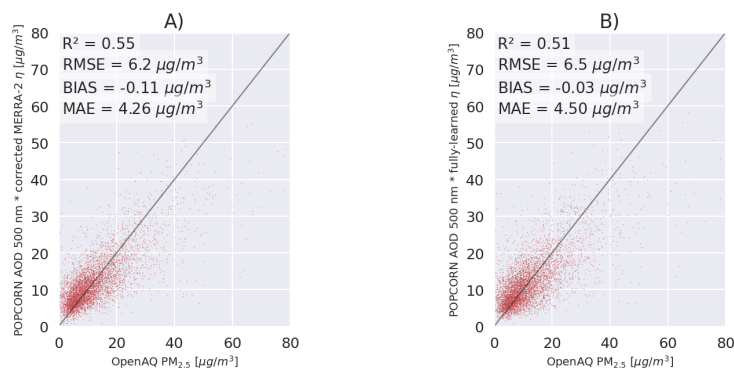


**Figure 1.** A) Post process corrected  $PM_{2.5}$  predictions against OpenAQ  $PM_{2.5}$  measurements. B) Fully-learned NOODLESALAD  $PM_{2.5}$  predictions against OpenAQ  $PM_{2.5}$  measurements.

25 the approach could be extended to more global training data and include data, for example, from India and China, where higher values of  $PM_{2.5}$  exist more frequently.

### 1.3 More information of satellite data is needed. What is the temporal resolution and swath of the sensor?

Two Sentinel-3 satellites currently flying provide revisit times of less than two days for OLCI and less than one day for the SLSTR instrument at equator. Swath width of the OLCI instrument is 1270 km. SLSTR swath width is 1420 km for the nadir view and 750 km for the oblique view. In our study, we base our aerosol information on the official Sentinel-3 Synergy Land data product and the characteristics of that data set matches our satellite overpass data. The information have been added to the manuscript.

### 1.4 This study only demonstrates the validations in Fig. 4. It would be more interesting to show the fitting (training) as well.

35 Fig.2 shows the results on the training set. The metrics are better than on the test set (as it is expected to be), but not very different since we used the early stopping technique as regularization to avoid overfitting on the training set. We remark that in this study we separated part of the available stations to be used as independent validation data for the methods. For operational use, the model could be trained using all the available data in the training and test data sets.

### 1.5 In Fig.4, why monthly mean shows larger bias than instant estimations?

40 It is not strictly necessary that the monthly bias is smaller than the instantaneous bias. We have added mean absolute error (MAE) as an additional metric in the figures. MAE shows improvement for the monthly data over the instantaneous data.



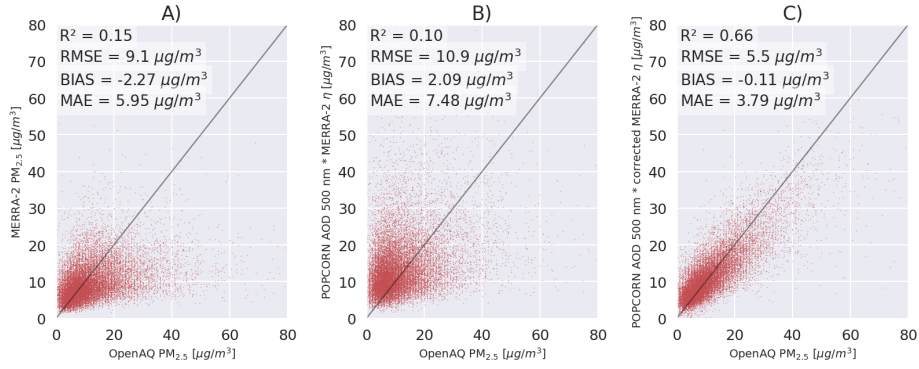


**Figure 2.** A) MERRA-2  $PM_{2.5}$  predictions against OpenAQ  $PM_{2.5}$  measurements per single-overpass. B) Uncorrected NODLESALAD  $PM_{2.5}$  predictions against OpenAQ  $PM_{2.5}$  measurements per single-overpass. C) Corrected NODLESALAD  $PM_{2.5}$  predictions against OpenAQ  $PM_{2.5}$  measurements per single-overpass. These results regard the training set.

### 1.6 Latitude and longitude are missing in the top panels of Figs. 5 and 6.

Latitude and longitude have been added to the panels.

### 1.7 Line 78-80: I cannot understand. More details are needed for the method description.

45 Some OpenAQ stations report 24 hour average  $PM_{2.5}$  every hour based on the last 24 hours.

In this work, we used the 24 hour averages given every hour to estimate hourly  $PM_{2.5}$ . This processing was done station-by-station using a Tikhonov regularized (with regularization parameter value 0.05) least-squares fit to unfold the time integrated data into hourly estimates.

In practice, the hourly  $PM_{2.5}$  estimates were computed using the formula

$$50 \quad PM_{2.5,1h} = (A^T A + \alpha I)^{-1} A^T b, \quad (1)$$

where the system matrix

$$A = \begin{bmatrix} \frac{1}{24} & \frac{1}{24} & \cdots & \frac{1}{24} & 0 & 0 & \cdots & 0 \\ 0 & \frac{1}{24} & \cdots & \frac{1}{24} & \frac{1}{24} & 0 & \cdots & 0 \\ & & & \vdots & & & & \\ 0 & 0 & \cdots & 0 & 0 & 0 & \cdots & \frac{1}{24} \end{bmatrix}, \quad (2)$$

is 24 hour time averaging operator and the data vector

$$b = \begin{bmatrix} PM_{2.5,24h,1} \\ PM_{2.5,24h,2} \\ \vdots \\ PM_{2.5,24h,N} \end{bmatrix}, \quad (3)$$

55

$$PM_{2.5,1h} = \begin{bmatrix} PM_{2.5,1h,24} \\ PM_{2.5,1h,25} \\ \vdots \\ PM_{2.5,1h,N} \end{bmatrix} \quad (4)$$

contain the hourly 24 hour averages  $PM_{2.5,24h,N}$  of the station data and  $\alpha = 0.05$  is the regularization parameter. The solution vector  $PM_{2.5,1h,N}$  contains the unfolded 1 hour  $PM_{2.5}$  at timestep  $N$ , respectively.

We have added this explanation in the revised manuscript.

60 **1.8 Why CALIOP data are used. This is monthly mean data, but  $PM_{2.5}$  and AOD has strong diurnal variation. Can the CALIOP data help to improve  $PM_{2.5}$  estimation?**

We tested the approach without CALIOP data in the training and the result is shown in fig.3 (left image: CALIOP included, right image: without CALIOP). The model which uses CALIOP data results in slightly better accuracy, indicating that use of CALIOP data is warranted.

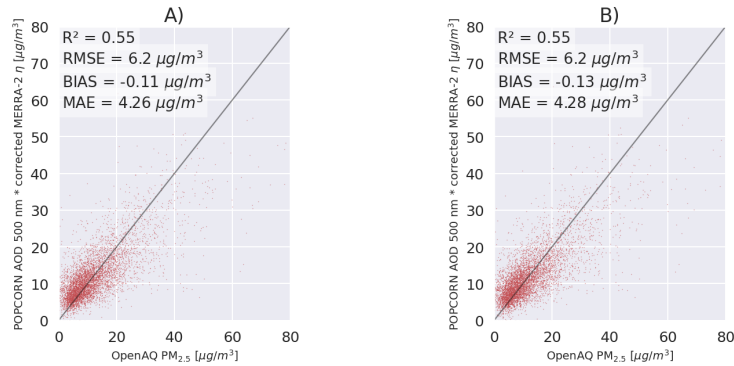


**Figure 3.** A) Corrected NOODLESALAD  $PM_{2.5}$  predictions against OpenAQ  $PM_{2.5}$  measurements per single-overpass (using CALIOP data). B) Corrected NOODLESALAD  $PM_{2.5}$  predictions against OpenAQ  $PM_{2.5}$  measurements per single-overpass (without CALIOP data).

65 **1.9 The unit of RMSE is missing throughout the paper.**

The unit of RMSE has been added to the paper.

**2 Answers to reviewer #2**

**2.1 Abstract: The study lacks major conclusions and quantitative descriptive results.**

The abstract has been modified as follows (extension highlighted in red):

70 Estimates of  $PM_{2.5}$  levels are crucial for monitoring air quality and studying the epidemiological impact of air quality on the population. Currently, the most precise measurements of  $PM_{2.5}$  are obtained from ground stations, resulting in limited spatial coverage. In this study, we consider satellite-based  $PM_{2.5}$  retrieval, which involves conversion of high-resolution satellite retrieval of Aerosol Optical Depth (AOD) into high-resolution  $PM_{2.5}$  retrieval. To improve the accuracy of the AOD to  $PM_{2.5}$  conversion, we employ the machine learning based post-process correction to correct the AOD-to-PM conversion ratio derived  
75 from Modern-Era Retrospective analysis for Research and Applications, Version 2 (MERRA-2) reanalysis model data. The post-process correction approach utilizes a fusion and downscaling of satellite observation and retrieval data, MERRA-2 reanalysis data, various high resolution geographical indicators, meteorological data and ground station observations for learning a predictor for the approximation error in the AOD to  $PM_{2.5}$  conversion ratio. The corrected conversion ratio is then applied to estimate  $PM_{2.5}$  levels given the high-resolution satellite AOD retrieval data derived from Sentinel-3 observations. **The region of  
80 study is central Europe during the year 2019. Our model produces  $PM_{2.5}$  estimates with a spatial resolution of 100 meters at satellite overpass times with  $R^2 = 0.55$  and  $RMSE = 6.2 \mu g/m^3$ . The corresponding metrics for monthly averages are  $R^2 = 0.72$  and  $RMSE = 3.7 \mu g/m^3$ .** Additionally, we have incorporated an ensemble of neural networks to provide error envelopes for machine learning related uncertainty in the  $PM_{2.5}$  estimates. **The proposed approach can produce accurate high resolution  $PM_{2.5}$  data that can be very useful for air quality monitoring, emission regulation and epidemiological studies.**

85 **2.2 The introduction is very short and lacks a comprehensive review of numerous previous studies on converting AOD to  $PM_{2.5}$  using machine learning models.**

The introduction has been modified as follows (extension highlighted in red):

Poor air quality is one of the most serious environmental health risks of our time. In September 2021, the World Health Organization (WHO) released Global Air Quality Guidelines, revealing clear evidence of the damage air pollution inflicts on  
90 human health at even lower concentrations than previously understood (World Health Organization, 2021). WHO estimates that exposure to air pollution causes 7 million premature deaths every year. A key indicator in monitoring air quality and epidemiological studies is the  $PM_{2.5}$  parameter, which is the dry mass concentration of fine particulate matter with an aerodynamic diameter of less than 2.5 micrometers (micrograms of particulate matter per cubic meter of air). Fine particulate matter originates from vehicle emissions, coal burning, and industrial emissions, among many other human and natural sources.  
95 Epidemiological studies link long exposures to high  $PM_{2.5}$  levels to many severe illnesses, such as stroke and cardiovascular

and respiratory diseases (e.g. Pope and Dockery, 2006; Cohen et al., 2017). On a global scale, the magnitude of the  $PM_{2.5}$  exposure-related risk for human health is enormous as more than 90% of the world's population lives in areas with annual mean  $PM_{2.5}$  levels exceeding the new WHO 2021 air quality guideline of 5 micrograms per cubic meter (Health Effects Institute, 2019).

100 While the knowledge of the health effects of pollution increases continuously, the epidemiological estimates still have significant uncertainties due to the lack of accurate global air pollution data (Hammer et al., 2020). Networks of ground-based observation stations produce accurate pointwise observations of  $PM_{2.5}$  and certain chemical components such as ozone, sulfur dioxide and nitrogen dioxide. These ground station measurements produce relatively accurate data, but the networks consist of only a few thousand irregularly located observation stations, mainly in developed countries, leading to the insufficient spatial  
105 coverage of the  $PM_{2.5}$  data. To better monitor and understand air quality and pollution sources near real-time global observations of air quality are needed. The only way to get spatially resolved air quality data is to utilize satellite retrievals.

Satellite retrievals of  $PM_{2.5}$  are often based on satellite AOD retrievals and AOD-to-PM conversion ratio (Health Effects Institute, 2019; van Donkelaar et al., 2013; Zhang and Kondragunta, 2021; Geng et al., 2015). AOD is a columnar optical quantity, whereas  $PM_{2.5}$  is the mass concentration of dry aerosol particles at some single point, typically at the surface level.  
110 Many factors affect the AOD-to-PM conversion ratio, including the aerosol vertical extinction profile, aerosol type and size distribution, and relative humidity. These factors are typically unavailable from a single data source, such as data provided by the instruments onboard a satellite, so a simulation-model-based AOD-to-PM ratio is often used. The simulation-model-based AOD-to-PM conversion ratio is typically computed based on meteorology, chemical transport models (CTM) and auxiliary satellite data such as lidar-based aerosol vertical profiles. The  $PM_{2.5}$  retrieval at a given location and time is then calculated as a  
115 product of the retrieved satellite AOD and the AOD to  $PM_{2.5}$  ratio. The current state-of-the-art  $PM_{2.5}$  retrieval algorithm also contains a post-processing step where the retrieved spatial  $PM_{2.5}$  estimate is fitted to the ground-based  $PM_{2.5}$  station data by a linear geographically weighted regression (van Donkelaar et al., 2016).

Many previous studies use machine learning techniques to convert AOD to  $PM_{2.5}$  levels. In particular, (Ibrahim et al., 2022) used a variant of Random Forest called Extremely Randomised Trees (ET) to estimate  $PM_{2.5}$  across Europe. (Stafoggia et al.,  
120 2019; Schneider et al., 2020) used Random Forest regressors in a multi-stage approach to estimate  $PM_{2.5}$  at ground stations when only  $PM_{10}$  measurements were available, to impute AOD values when not accessible and to finally predict  $PM_{2.5}$  values across Italy and Great Britain. (Handschuh et al., 2023) considered multiple Random Forest models to evaluate  $PM_{2.5}$  levels across Germany using 4 different AOD datasets.

In this paper, we propose a novel approach for high-resolution satellite-based retrieval of  $PM_{2.5}$ . While the previous studies  
125 use machine learning to learn the AOD to  $PM_{2.5}$  conversion directly, we take a novel approach where we train the model to predict the approximation error in the geophysical model based conversion ratio. Our approach retrieves  $PM_{2.5}$  at the spatial resolution of 100 m. It is based on the machine learning post-process correction approach, which we developed for the correction of approximation errors in satellite retrievals (Lipponen et al., 2021) and employed for high-resolution spectral aerosol optical depth (AOD) retrieval (POPCORN AOD) from SENTINEL-3 SYNERGY data (Lipponen et al., 2022). In our algorithm  
130 development work, we take the spectral, high-resolution Sentinel-3 POPCORN AOD (Lipponen et al., 2022) as the starting point.

Our  $PM_{2.5}$  retrieval is based on the AOD-to- $PM_{2.5}$  conversion ratio applied to the POPCORN AOD. The AOD-to- $PM_{2.5}$  ratio is estimated by machine learning techniques utilizing a fusion of collocated ground station-based in-situ  $PM_{2.5}$  data, MERRA-2 reanalysis model AOD and  $PM_{2.5}$  data, spectral AERONET AOD, satellite-observed spectral top-of-atmosphere reflectances, meteorology data and various high-resolution geographical indicators representing, for example, population density and land surface elevation. Utilizing these data, we employ the post-process correction approach to the estimation of AOD-to- $PM_{2.5}$  ratio (Lipponen et al., 2021, 2022; Taskinen et al., 2022) and then the high-resolution  $PM_{2.5}$  retrieval is obtained as the product of the post-process corrected AOD-to- $PM_{2.5}$  ratio and POPCORN AOD. By using an ensemble of neural networks, we can also provide error envelopes for the machine learning related uncertainty in the  $PM_{2.5}$  estimates. The approach is tested with Sentinel-3 data from central Europe in 2019.

140 **2.3 The use of MERRA2-2 for calculating  $PM_{2.5}$  is criticized for its inaccuracies and omission of certain species like Nitrate. It is suggested to consider using GEOS-CF data, which provides  $PM_{2.5}$  simulations at a higher resolution of 0.25 degrees.**

We thank the referee for the suggestion. We agree that GEOS-CF would be a suitable and good model data to consider in our methodology. Our methodology developed is not restricted to any single model or satellite data. Some criteria in selecting the model data for our work were long time series and widely used model in scientific literature and we therefore ended up selecting MERRA-2. In our future work, we will consider using GEOS-CF data as it has somewhat better spatial accuracy and more relevant species for air quality applications.

**2.4 The spatial resolution of high-resolution indicators such as roads and nighttime lights needs clarification.**

- NASA Black Marble Night Lights: We use the 500 meter resolution data.
- 150 – OpenStreetMap roads: The original data is vector data with a typical accuracy of orders of meters. We have re-projected the OpenStreetMap road data to 100 meter resolution before use.

We have added the resolutions used to the revised manuscript.

**2.5 The excessive number of variables selected raises questions about their relevance and contribution to the network model. It would be beneficial to employ importance analysis methods to identify and eliminate redundant variables. This process will streamline the model and improve its efficiency and interpretability.**

We used SHAP analysis (Lundberg and Lee (2017)) to estimate the feature importance after model training. A bar plot can be seen in fig.4 for the first 26 features found with the SHAP analysis. Table 1 contains all the input variables listed by importance (SHAP value). Since all the variables had non-negligible SHAP values, indicating some information content in them, we decided to keep them all. The input variable table in the manuscript has been modified so that now the variables are listed in order of importance by the SHAP values.

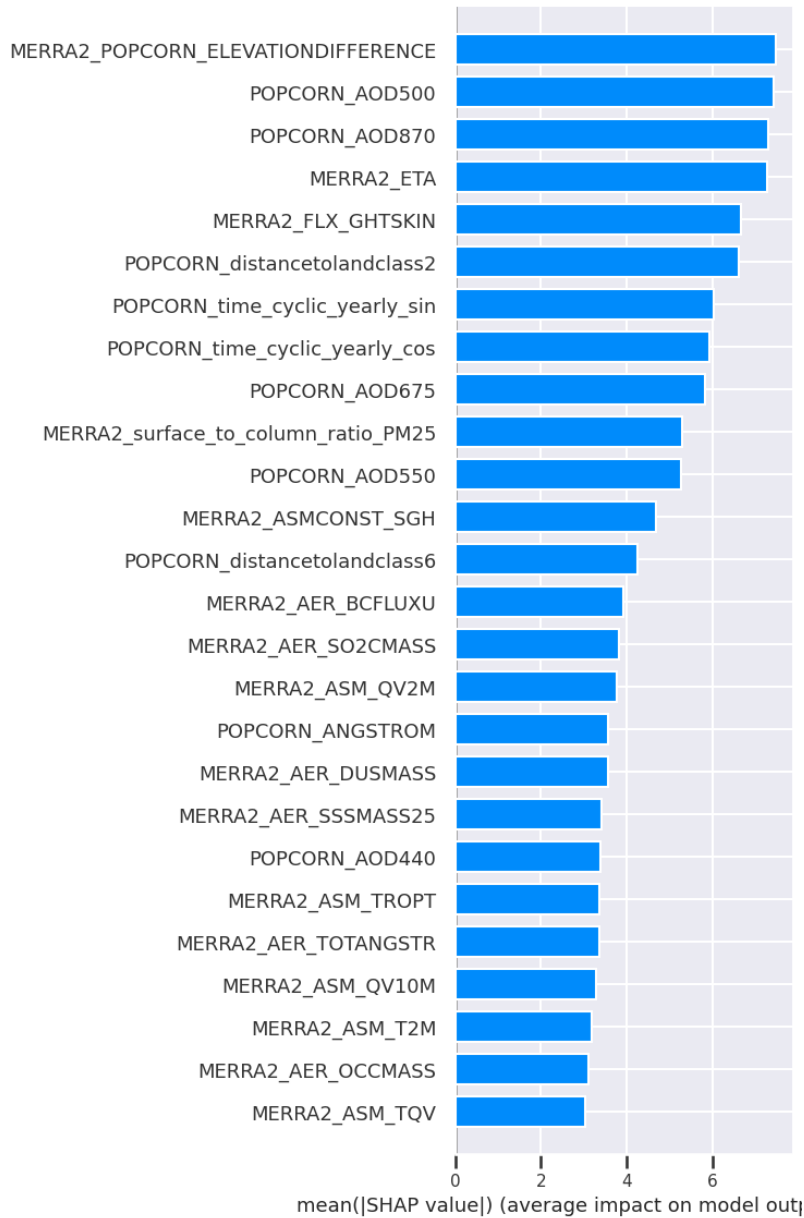


**Figure 4.** Bar plot of the SHAP values for the first 26 input variables in order of importance.

**2.6 Figure 3: It is unclear how the training and validation stations are divided. Additionally, the proximity of stations may lead to correlation issues, affecting the independence of training and testing samples spatially.**

We are not the first ones to use site-validation, please see the review of different validation methods used in the literature Tang et al. (2024). Essentially we divided randomly the stations into training set, validation set and test set, then used the related data

165 accordingly. For what regards the correlation issues, there should be only a minimal effect since we are operating at resolution of 100 m and there are not two or more stations in the same pixel.

**2.7 Section 3.4: The rationale for choosing the neural network model over other more powerful machine learning and deep learning models is not provided. The advantages of this model should be discussed.**

Using a fully connected neural network compared to other common models in  $PM_{2.5}$  prediction like random forest is very  
170 suitable in the case one is working with assumption of independent pixels and a high number of data samples and features. In this case, our study is limited to the chosen ROI and period of time (2019) so we have roughly 20000 points in the training set: our plan is to extend the ROI and the period of time in future studies so to have more data in the training set, where the fully connected neural network should show all its learning capability. Comparing the fully connected neural network to other deep learning models, we think it is the most suitable architecture for the task at hand since we are dealing with tabular data and a fair  
175 amount of features. One could for example think of using a convolutional neural network and reorganizing the data samples into appropriate matrices but still the number of features is small and we don't know if we would benefit deploying a convolutional network (there's no computational burden to justify this approach and the fully connected neural network should be able to find proper representations of the input data in its hidden layers).

**2.8 Figure 4: While the accuracy has improved, the correlation remains relatively low (only 0.63), compared to  
180 previous studies achieving higher accuracy with AI (R2 higher than 0.8). The significance of the study is questioned, and comparison with previous studies to assess improvement is recommended.**

The  $R^2$  coefficient is low compared to other studies but we should compare our manuscript to papers who deal with, for example, the same ROI, spatial resolution and study time period. Our RMSE is comparable to other studies that consider European countries or similar ROI (Schneider et al. (2020); Ibrahim et al. (2022); Handschuh et al. (2023)). The  $R^2$  coefficient is low  
185 but the number of data samples at hand is low too: as mentioned before, we are considering the year 2019 and compared, for example, to Ibrahim et al. (2022) we have 10% of data. Our ensemble of fully connected neural networks would benefit from having more data and the metrics would improve further. Also the data and the preprocessing choices are different, so the studies are not directly comparable.

MERRA2_POPCORN_ELEVATIONDIFFERENCE	POPCORN_AOD500	POPCORN_AOD870
MERRA2_ETA	MERRA2_FLX_GHTSKIN	POPCORN_distancetolandclass2
POPCORN_time_cyclic_yearly_sin	POPCORN_time_cyclic_yearly_cos	POPCORN_AOD675
MERRA2_surface_to_column_ratio_PM25	POPCORN_AOD550	MERRA2_ASMCONST_SGH
POPCORN_distancetolandclass6	MERRA2_AER_BCFLUXU	MERRA2_AER_SO2CMASS
MERRA2_ASM_QV2M	POPCORN_ANGSTROM	MERRA2_AER_DUSMASS
MERRA2_AER_SSSMASS25	POPCORN_AOD440	MERRA2_ASM_TROPT
MERRA2_AER_TOTANGSTR	MERRA2_ASM_QV10M	MERRA2_ASM_T2M
MERRA2_AER_OCCMASS	MERRA2_ASM_TQV	MERRA2_FLX_QLML
MERRA2_AER_SUFLUXV	MERRA2_FLX_USTAR	MERRA2_AER_SO4CMASS
POPCORN_distancetolandclass17	MERRA2_AER_DUCMASS	MERRA2_AER_BCSMASS
MERRA2_AER_BCSCATAU	MERRA2_AER_DUEXTTAU	MERRA2_FLX_EFLUX
MERRA2_AER_SO4SMASS	MERRA2_FLX_EVAP	MERRA2_FLX_NIRDR
MERRA2_FLX_HFLUX	POPCORN_ASTERDEM	MERRA2_AER_SUANGSTR
MERRA2_ASM_TROPPB	MERRA2_AER_BCFLUXV	MERRA2_FLX_TLML
MERRA2_FLX_QSTAR	POPCORN_time_cyclic_daily_sin	MERRA2_AER_DUSCATAU
MERRA2_FLX_PBLH	POPCORN_distancetolandclass7	POPCORN_distancetolandclass12
MERRA2_AER_OCSCATAU	MERRA2_AER_TOTEXTTAU	POPCORN_distancetolandclass15
MERRA2_ASM_TROPPV	MERRA2_SURFACERH	MERRA2_FLX_RHOA
MERRA2_AER_BCEXTTAU	MERRA2_FLX_FRCLS	MERRA2_AER_DUEXTT25
MERRA2_ASM_T10M	MERRA2_ASM_TS	MERRA2_FLX_SPEED
MERRA2_AER_BCANGSTR	MERRA2_AER_DUSCAT25	MERRA2_AER_OCFLUXU
MERRA2_CTMCONST_FRLANDICE	MERRA2_AER_DUCMASS25	MERRA2_AER_OCEXTTAU
MERRA2_FLX_FRCAN	MERRA2_ASMCONST_FRLAND	MERRA2_AER_SSCMASS
MERRA2_AER_TOTSCATAU	MERRA2_AER_BCCMASS	MERRA2_CTMCONST_FRACI
MERRA2_AER_DUSMASS25	POPCORN_distancetolandclass16	POPCORN_CALIOP_MASK_AOD_90_Percent_Below
POPCORN_time_cyclic_daily_cos	POPCORN_distancetolandclass4	MERRA2_AER_DUANGSTR
MERRA2_FLX_SPEEDMAX	MERRA2_CTMCONST_FRLAND	MERRA2_FLX_HLML
MERRA2_AER_DUFLUXV	MERRA2_AER_OCANGSTR	MERRA2_FLX_TAUY
MERRA2_FLX_FRCCN	MERRA2_PM25	MERRA2_ASMCONST_FRLAKE
POPCORN_distancetolandclass8	MERRA2_AER_SSFLUXV	MERRA2_AER_SUFLUXU
MERRA2_FLX_CDQ	POPCORN_distancetolandclass13	MERRA2_FLX_TSTAR
MERRA2_FLX_CN	MERRA2_ASM_V50M	MERRA2_AER_SSSCATAU
MERRA2_FLX_QSH	MERRA2_FLX_Z0H	MERRA2_ASM_PS
MERRA2_AER_SSEXTTAU	MERRA2_FLX_TCZPBL	MERRA2_AER_OCSMASS
MERRA2_FLX_TSH	POPCORN_distancetolandclass3	MERRA2_SURFACEELEVATION
MERRA2_ASM_TROPQ	MERRA2_FLX_CDH	MERRA2_FLX_PGENTOT
MERRA2_ASM_U10M	MERRA2_FLX_ULML	MERRA2_ASM_TOX
MERRA2_AER_DMSSMASS	POPCORN_distancetolandclass1	POPCORN_distancetolandclass14
MERRA2_FLX_TAUX	MERRA2_ASMCONST_FRLANDICE	MERRA2_AER_SUSCATAU
MERRA2_AER_DUFLUXU	POPCORN_distancetolandclass10	MERRA2_FLX_PREVTOT
MERRA2_CTMCONST_FROCEAN	MERRA2_ASM_TQL	MERRA2_ASM_U2M
MERRA2_ASM_DISP	MERRA2_FLX_PRECTOT	MERRA2_AER_SO2SMASS
MERRA2_FLX_CDM	MERRA2_FLX_Z0M	MERRA2_ASM_windspeed
POPCORN_distancetolandclass11	MERRA2_FLX_DISP	MERRA2_AER_OCFLUXV
MERRA2_FLX_PRECTOTCORR	MERRA2_ASM_TROPPT	MERRA2_FLX_PRECLSC
MERRA2_FLX_BSTAR	MERRA2_ASM_TO3	POPCORN_CALIOP_MASK_AOD_63_Percent_Below
MERRA2_FLX_PRECCON	MERRA2_ASM_TQI	MERRA2_ASMCONST_FROCEAN
MERRA2_CTMCONST_PHIS	POPCORN_distancetolandclass5	MERRA2_CTMCONST_FRLAKE
MERRA2_FLX_TAUWX	MERRA2_FLX_PRECANV	MERRA2_ASM_V2M
MERRA2_ASMCONST_PHIS	MERRA2_FLX_NIRDF	POPCORN_distancetolandclass9
MERRA2_ASM_SLP	POPCORN_BlackMarble	POPCORN_distancetoroad_upwind
MERRA2_AER_SSANGSTR	MERRA2_FLX_VLML	MERRA2_AER_SSSCAT25
MERRA2_ASM_winddirection	MERRA2_FLX_TAUWY	MERRA2_AER_SFLUXU
MERRA2_AER_SUEXTTAU	MERRA2_ASM_V10M	MERRA2_AER_SSCMASS25
MERRA2_FLX_PRECSNO	MERRA2_AER_SSEXTT25	MERRA2_AER_DMSSMASS
MERRA2_FLX_RISFC	MERRA2_AER_SSSMASS	MERRA2_ASM_U50M
MERRA2_FLX_FRSEAICE		

**Table 1.** List of input variables used in our model ordered by SHAP value (from left to right and from top to bottom).



## References

- 190 Cohen, A. J., Brauer, M., Burnett, R., Anderson, H. R., Frostad, J., Estep, K., et al.: Estimates and 25-year trends of the global burden of disease attributable to ambient air pollution: an analysis of data from the Global Burden of Diseases Study 2015, *The Lancet*, 389, 1907–1918, 2017.
- Geng, G., Zhang, Q., Martin, R., Donkelaar, A., Huo, H., CHE, H., Lin, J., and He, H.: Estimating long-term PM<sub>2.5</sub> concentrations in China using satellite-based aerosol optical depth and a chemical transport model, *Remote Sensing of Environment*, 166, 195 <https://doi.org/10.1016/j.rse.2015.05.016>, 2015.
- Hammer, M. S., van Donkelaar, A., Li, C., Lyapustin, A., Sayer, A. M., Hsu, N. C., Levy, R. C., Garay, M. J., Kalashnikova, O. V., Kahn, R. A., et al.: Global estimates and long-term trends of fine particulate matter concentrations (1998–2018), *Environmental Science & Technology*, 54, 7879–7890, 2020.
- Handschuh, J., Erbertseder, T., and Baier, F.: Systematic Evaluation of Four Satellite AOD Datasets for Estimating PM<sub>2.5</sub> Using a Random Forest Approach, *Remote Sensing*, 15, <https://doi.org/10.3390/rs15082064>, 2023.
- 200 Health Effects Institute: State of global air 2019, 2019.
- Ibrahim, S., Landa, M., Pešek, O., Brodský, L., and Halounová, L.: Machine Learning-Based Approach Using Open Data to Estimate PM<sub>2.5</sub> over Europe, *Remote Sensing*, 14, <https://doi.org/10.3390/rs14143392>, 2022.
- Lipponen, A., Kolehmainen, V., Kolmonen, P., Kukkurainen, A., Mielonen, T., Sabater, N., Sogacheva, L., Virtanen, T. H., and Arola, A.: 205 Model-enforced post-process correction of satellite aerosol retrievals, *Atmospheric Measurement Techniques*, 14, 2981–2992, 2021.
- Lipponen, A., Reinval, J., Väisänen, A., Taskinen, H., Lähivaara, T., Sogacheva, L., Kolmonen, P., Lehtinen, K., Arola, A., and Kolehmainen, V.: Deep-learning-based post-process correction of the aerosol parameters in the high-resolution Sentinel-3 Level-2 Synergy product, *Atmospheric Measurement Techniques*, 15, 895–914, 2022.
- Lundberg, S. M. and Lee, S.: A unified approach to interpreting model predictions, *CoRR*, abs/1705.07874, <http://arxiv.org/abs/1705.07874>, 210 2017.
- Pope, C. A. I. and Dockery, D. W.: Health Effects of Fine Particulate Air Pollution: Lines that Connect, *Journal of the Air & Waste Management Association*, 56, 709–742, <https://doi.org/10.1080/10473289.2006.10464485>, 2006.
- Schneider, R., Vicedo-Cabrera, A. M., Sera, F., Masselot, P., Stafoggia, M., de Hoogh, K., Kloog, I., Reis, S., Vieno, M., and Gasparri, A.: A Satellite-Based Spatio-Temporal Machine Learning Model to Reconstruct Daily PM<sub>2.5</sub> Concentrations across Great Britain, *Remote Sensing*, 12, <https://doi.org/10.3390/rs12223803>, 2020.
- 215 Stafoggia, M., Bellander, T., Bucci, S., Davoli, M., de Hoogh, K., de' Donato, F., Gariazzo, C., Lyapustin, A., Michelozzi, P., Renzi, M., Scortichini, M., Shtein, A., Viegi, G., Kloog, I., and Schwartz, J.: Estimation of daily PM<sub>10</sub> and PM<sub>2.5</sub> concentrations in Italy, 2013–2015, using a spatiotemporal land-use random-forest model, *Environment International*, 124, 170–179, <https://doi.org/https://doi.org/10.1016/j.envint.2019.01.016>, 2019.
- 220 Tang, D., Zhan, Y., and Yang, F.: A review of machine learning for modeling air quality: Overlooked but important issues, *Atmospheric Research*, 300, 107 261, <https://doi.org/https://doi.org/10.1016/j.atmosres.2024.107261>, 2024.
- Taskinen, H., Väisänen, A., Hatakka, L., Virtanen, T. H., Lähivaara, T., Arola, A., Kolehmainen, V., and Lipponen, A.: High-Resolution Post-Process Corrected Satellite AOD, *Geophysical Research Letters*, 49, e2022GL099 733, 2022.
- van Donkelaar, A., Martin, R. V., Spurr, R. J., Drury, E., Remer, L. A., Levy, R. C., and Wang, J.: Optimal estimation for global ground-level 225 fine particulate matter concentrations, *Journal of Geophysical Research: Atmospheres*, 118, 5621–5636, 2013.

- van Donkelaar, A., Martin, R. V., Brauer, M., Hsu, N. C., Kahn, R. A., Levy, R. C., Lyapustin, A., Sayer, A. M., and Winker, D. M.: Global Estimates of Fine Particulate Matter using a Combined Geophysical-Statistical Method with Information from Satellites, Models, and Monitors, *Environmental Science & Technology*, 50, 3762–3772, <https://doi.org/10.1021/acs.est.5b05833>, 2016.
- World Health Organization: New WHO Global Air Quality Guidelines aim to save millions of lives from air pollution, <https://www.who.int/news/item/22-09-2021-new-who-global-air-quality-guidelines-aim-to-save-millions-of-lives-from-air-pollution>, [Online; accessed 12-April-2023], 2021.
- Xu, L., Skoularidou, M., Cuesta-Infante, A., and Veeramachaneni, K.: Modeling Tabular data using Conditional GAN, 2019.
- Zhang, H. and Kondragunta, S.: Daily and Hourly Surface PM<sub>2.5</sub> Estimation From Satellite AOD, *Earth and Space Science*, 8, e2020EA001 599, <https://doi.org/https://doi.org/10.1029/2020EA001599>, e2020EA001599 2020EA001599, 2021.

# Post-process correction improves the accuracy of satellite PM<sub>2.5</sub> retrievals manuscript - Reply to Adam Povey, Supriya Mantri and Laura Horton

Andrea Porcheddu, Ville Kolehmainen, Timo Lähivaara, Antti Lipponen

We would like to thank you for reading the manuscript and giving comments. Below we answer to each of the comments.

## 1 Answers

**1.1 The introduction was clear with good motivations and references but, in line 25, the reference to the WHO air quality guideline does not specify the time frame. Is it an annual average?**

5 Yes, it is an annual average.

**1.2 Is it possible to give any additional reasoning behind the use of hourly downscaling of daily PM averages? This strikes us as one of the more consequential choices in this methodology and neglects complexities such as the diurnal cycle. (We aren't questioning the authors' judgement, nor disagreeing; merely curious as we wouldn't have thought of this.)**

10 We are simply unrolling 24h averages given every hour, so the hourly measurements information is contained in each 24h average.

**1.3 In section 2.3 the authors mention they use MERRA-2 reanalysis variables as an input for the model and provide a lengthy list in the appendix. Have all of the available variables been used as an input or are there some variables not included? It may be helpful for those designing similar algorithms if you also mention which variables were not included and, if so, why not?**

15

A table with all the features used in the training of the model is available at the end of the manuscript. We have used all the MERRA-2 reanalysis variables mentioned in the table. We have also carried out SHAP analysis that showed us that all MERRA-2 input variables were informative and had non-negligible effect on the model output.

**1.4 Could you provide a reference for the RH equation on line 93? Or is it at standard temperature/pressure?**

20 The RH equation is based on the Clausius-Clapeyron equation. We have now mentioned the Clausius-Clapeyron equation and included a reference to a paper using the formula and having more information about the equation in the revised manuscript.

**1.5 In the NASA Black Marble Night Light section (2.6.2), the authors could include a reference to the data set used, especially a DOI so we can distinguish which of the four available datasets was used.**

We have added a reference to the dataset in the revised manuscript.

25 **1.6 We found Sections 3.3 and 3.4 quite opaque. They could be improved by adding more specific details about the process, such as the equations used as an input to the correction model. A flow chart of the steps used in the approach would make it more clear for an audience which is less familiar with machine learning and neural networks.**

The sections have been improved adding some more equations and explanations of their content.

30 **1.7 Those of us with little experience with neural networks did not understand what Figure 2 wished to convey and those of us used to neural networks felt Figure 2 adds little to the text; it could be removed.**

Thank you for the suggestion but we decided to keep the figure since we think it could be informative.

**1.8 At line 183, it would be helpful to have an understanding of what is meant by “slightly better”?**

We modified the text from "slightly better" to "better".

35 **1.9 Figure 3 could be improved as it is hard to distinguish between lines, perhaps using a filled histogram of stacked bars.**

We modified the plot with thicker lines and no transparency for the colors.

**1.10 We are curious if the authors considered any methods to amplify the availability of high PM2.5 observations, such as data augmentation? Our understanding was that the balancing of training data is an important step in constructing a neural network to recognise rare events and we would value the authors’ opinion.**

We have tested augmenting the data using CTGAN (Conditional Tabular Generative Adversarial Network) and TVAE (Tabular Variational Auto Encoder) (Xu et al., 2019) but didn’t observe any improvement.

**1.11 From line 223, what do you mean by “the fully learned approach were less accurate than with the post correction approach”? What metric of accuracy was used and how significant was the difference? This would help guide our own efforts in neural network generation.**

We calculated different metrics including  $R^2$ , RMSE and MAE. In particular, for the post-correction approach we obtained  $R^2=0.55$ , RMSE= $6.2 \mu\text{g}/\text{m}^3$  and MAE= $4.26 \mu\text{g}/\text{m}^3$ , while for the fully-learned approach we obtained  $R^2=0.51$ , RMSE= $6.5 \mu\text{g}/\text{m}^3$  and MAE= $4.50 \mu\text{g}/\text{m}^3$ .

50 **1.12 In Figure 4, are the authors certain about the plotting of panel B? Compared to panel A there appears to be some duplication of points up the y-axis. For example, there are three points at the extreme right of (A) but over ten in (B). This effect is not exhibited in panels D-F.**

Yes, we are sure about the plotting. We checked further and we found no problems.

55 **1.13 In Figure 5 (comparison of the uncorrected and corrected methods at the ground stations), do the authors have any understanding of why there is a large discrepancy between OpenAQ and both satellite estimates for most of the sites (i.e. the blue dots do not overlap the red line in 5/9 cases shown). Is it because of some local source (e.g. roads or small industrial buildings) in close proximity of the stations that isn't present in Madrid?**

We looked at the correlations between input features and errors and we didn't find any single feature that could explain the errors for the shown satellite overpass. Please note that the monthly averages for the test station in Paris are well aligned with the ground based data.

60 **1.14 In Figures 5 and 6, could the dots representing sites and arrows indicating one be made substantially larger and outlined with a colour not in the plot (such as green or blue)? Our older member had failed to see them on his own.**

The figures have been modified now, we chose green colour and larger arrow/font.

**1.15 In Figure 7 bottom left (Hull Freetown) why is the uncertainty so large April? What are the possible reasons for high PM<sub>2.5</sub> in February?**

65 We don't have any explanation for the large uncertainty in April: we looked at correlations between errors and input data but we didn't find anything interesting. For what regards the high PM<sub>2.5</sub> in February, it could be caused by the lower boundary layer height in winter months (as other causes like house heating, etc.).

70 **1.16 If practical, it would be interesting to add an appendix highlighting a few ensemble members for Fig 5 and/or 6. This would demonstrate if the smoothness of the fields shown at the top right of those figures is due to the action of the neural network or due to the median filter over the ensemble.**

The smoothness of the fields is not due to the median filter since the same smoothness can be seen in the figure regarding the not-corrected method (where no median filter is applied).

75 **1.17 It would be interesting to hear if training the model over an area with higher PM<sub>2.5</sub> levels, such as South Africa or India, and then testing over central Europe improves the model's performance, particularly for higher PM<sub>2.5</sub> values.**

That's our plan for future studies, we are curious to see if gathering more data from all around the world could improve the modelling in Europe.

## References

Xu, L., Skoularidou, M., Cuesta-Infante, A., and Veeramachaneni, K.: Modeling Tabular data using Conditional GAN, 2019.

# Post-process correction improves the accuracy of satellite PM<sub>2.5</sub> retrievals

Andrea Porcheddu<sup>1</sup>, Ville Kolehmainen<sup>1</sup>, Timo Lähivaara<sup>1</sup>, and Antti Lipponen<sup>2</sup>

<sup>1</sup>Department of Technical Physics, University of Eastern Finland, Kuopio, Finland

<sup>2</sup>Finnish Meteorological Institute, Atmospheric Research Centre of Eastern Finland, Kuopio, Finland

**Correspondence:** Andrea Porcheddu (andrea.porcheddu@uef.fi)

**Abstract.** Estimates of PM<sub>2.5</sub> levels are crucial for monitoring air quality and studying the epidemiological impact of air quality on the population. Currently, the most precise measurements of PM<sub>2.5</sub> are obtained from ground stations, resulting in limited spatial coverage. In this study, we consider satellite-based PM<sub>2.5</sub> retrieval, which involves conversion of high-resolution satellite retrieval of Aerosol Optical Depth (AOD) into high-resolution PM<sub>2.5</sub> retrieval. To improve the accuracy of the AOD to PM<sub>2.5</sub> conversion, we employ the machine learning based post-process correction to correct the AOD-to-PM conversion ratio derived from Modern-Era Retrospective analysis for Research and Applications, Version 2 (MERRA-2) reanalysis model data. The post-process correction approach utilizes a fusion and downscaling of satellite observation and retrieval data, MERRA-2 reanalysis data, various high resolution geographical indicators, meteorological data and ground station observations for learning a predictor for the approximation error in the AOD to PM<sub>2.5</sub> conversion ratio. The corrected conversion ratio is then applied to estimate PM<sub>2.5</sub> levels given the high-resolution satellite AOD retrieval data derived from Sentinel-3 observations. [The region of study is central Europe during the year 2019.](#) Our model produces PM<sub>2.5</sub> estimates with a spatial resolution of 100 meters at satellite overpass times [with  \$R^2 = 0.55\$  and RMSE =  \$6.2 \mu\text{g}/\text{m}^3\$ .](#) [The corresponding metrics for monthly averages are  \$R^2 = 0.72\$  and RMSE =  \$3.7 \mu\text{g}/\text{m}^3\$ .](#) Additionally, we have incorporated an ensemble of neural networks to provide error envelopes for machine learning related uncertainty in the PM<sub>2.5</sub> estimates. [The proposed approach can produce accurate high resolution PM<sub>2.5</sub> data that can be very useful for air quality monitoring, emission regulation and epidemiological studies.](#)

## 1 Introduction

Poor air quality is one of the most serious environmental health risks of our time. In September 2021, the World Health Organization (WHO) released Global Air Quality Guidelines, revealing clear evidence of the damage air pollution inflicts on human health at even lower concentrations than previously understood (World Health Organization, 2021). WHO estimates that exposure to air pollution causes 7 million premature deaths every year. A key indicator in monitoring air quality and epidemiological studies is the PM<sub>2.5</sub> parameter, which is the dry mass concentration of fine particulate matter with an aerodynamic diameter of less than 2.5 micrometers (micrograms of particulate matter per cubic meter of air). Fine particulate matter originates from vehicle emissions, coal burning, and industrial emissions, among many other human and natural sources. Epidemiological studies link long exposures to high PM<sub>2.5</sub> levels to many severe illnesses, such as stroke and cardiovascular and respiratory

25 diseases (e.g. Pope and Dockery, 2006; Cohen et al., 2017). On a global scale, the magnitude of the  $PM_{2.5}$  exposure-related risk for human health is enormous as more than 90% of the world's population lives in areas with annual mean  $PM_{2.5}$  levels exceeding the new WHO 2021 air quality guideline of 5 micrograms per cubic meter (Health Effects Institute, 2019).

While the knowledge of the health effects of pollution increases continuously, the epidemiological estimates still have significant uncertainties due to the lack of accurate global air pollution data (Hammer et al., 2020). Networks of ground-based  
30 observation stations produce accurate pointwise observations of  $PM_{2.5}$  and certain chemical components such as ozone, sulfur dioxide and nitrogen dioxide. These ground station measurements produce relatively accurate data, but the networks consist of only a few thousand irregularly located observation stations, mainly in developed countries, leading to the insufficient spatial coverage of the  $PM_{2.5}$  data. To better monitor and understand air quality and pollution sources near real-time global observations of air quality are needed. The only way to get spatially resolved air quality data is to utilize satellite retrievals.

35 Satellite retrievals of  $PM_{2.5}$  are often based on satellite AOD retrievals and [an](#) AOD-to-PM conversion ratio (Health Effects Institute, 2019; van Donkelaar et al., 2013; Zhang and Kondragunta, 2021; Geng et al., 2015). AOD is a columnar optical quantity, whereas  $PM_{2.5}$  is the mass concentration of dry aerosol particles at some single point, typically at the surface level. Many factors affect the AOD-to-PM conversion ratio, including the aerosol vertical extinction profile, aerosol type and size distribution, and relative humidity. These factors are typically unavailable from a single data source, such as data provided by  
40 the instruments onboard a satellite, so a simulation-model-based AOD-to-PM ratio is often used. The simulation-model-based AOD-to-PM conversion ratio is typically computed based on meteorology, chemical transport models (CTM) and auxiliary satellite data such as lidar-based aerosol vertical profiles. The  $PM_{2.5}$  retrieval at a given location and time is then calculated as a product of the retrieved satellite AOD and the AOD to  $PM_{2.5}$  ratio. The current state-of-the-art  $PM_{2.5}$  retrieval algorithm also contains a post-processing step where the retrieved spatial  $PM_{2.5}$  estimate is fitted to the ground-based  $PM_{2.5}$  station data  
45 by a linear geographically weighted regression (van Donkelaar et al., 2016).

[Many previous studies use machine learning techniques to convert AOD to  \$PM\_{2.5}\$  levels. In particular, \(Ibrahim et al., 2022\) used a variant of Random Forest called Extremely Randomised Trees \(ET\) to estimate  \$PM\_{2.5}\$  across Europe. \(Stafoggia et al., 2019; Schneid](#)  
[used Random Forest regressors in a multi-stage approach to estimate  \$PM\_{2.5}\$  at ground stations when only  \$PM\_{10}\$  measurements were available, to impute AOD values when not accessible and to finally predict  \$PM\_{2.5}\$  values across Italy and Great Britain.](#)  
50 [\(Handschuh et al., 2023\) considered multiple Random Forest models to evaluate  \$PM\_{2.5}\$  levels across Germany using 4 different AOD datasets.](#)

In this paper, we propose a novel approach for high-resolution satellite-based retrieval of  $PM_{2.5}$ . [While the previous studies use machine learning to learn the AOD to  \$PM\_{2.5}\$  conversion directly, we take a novel approach where we train the model to predict the approximation error in the geophysical model based conversion ratio.](#) Our approach retrieves  $PM_{2.5}$  at **the a**  
55 spatial resolution of 100 m. It is based on the machine learning post-process correction approach, which we developed for the correction of approximation errors in satellite retrievals (Lipponen et al., 2021) and employed for high-resolution spectral aerosol optical depth (AOD) retrieval (POPCORN AOD) from SENTINEL-3 SYNERGY data (Lipponen et al., 2022). In our algorithm development work, we take the spectral, high-resolution Sentinel-3 POPCORN AOD (Lipponen et al., 2022) as the starting point. Our  $PM_{2.5}$  retrieval is based on the AOD-to- $PM_{2.5}$  conversion ratio applied to the POPCORN AOD. The



60 AOD-to-PM<sub>2.5</sub> ratio is estimated by machine learning techniques utilizing a fusion of collocated ground station-based in-situ  
PM<sub>2.5</sub> data, MERRA-2 reanalysis model AOD and PM<sub>2.5</sub> data, spectral AERONET AOD, satellite-observed spectral top-  
of-atmosphere reflectances, meteorology data and various high-resolution geographical indicators representing, for example,  
population density and land surface elevation. Utilizing these data, we employ the post-process correction approach to the  
estimation of [the](#) AOD-to-PM<sub>2.5</sub> ratio (Lipponen et al., 2021, 2022; Taskinen et al., 2022) and then the high-resolution PM<sub>2.5</sub>  
65 retrieval is obtained as the product of the post-process corrected AOD-to-PM<sub>2.5</sub> ratio and POPCORN AOD. By using an  
ensemble of neural networks, we can also provide error envelopes for the machine learning related uncertainty in the PM<sub>2.5</sub>  
estimates. The approach is tested with Sentinel-3 data from central Europe in 2019.

## 2 Data

We use various input data variables in computing the estimate for the surface PM<sub>2.5</sub>. We use satellite observation data and  
70 retrievals, in-situ observations, and reanalysis model data. This section lists all the variables and data sources used in our work.

### 2.1 Sentinel-3 POPCORN AOD

[The](#) Sentinel-3 POPCORN AOD product is based on [the](#) post-process corrected Sentinel-3 SYNERGY land AOD product. It  
offers a spatial resolution of 300 meters and is currently accessible for Sentinel-3A and 3B overpasses, covering five regions of  
interest for the year 2019: Central Europe, Eastern USA, Western USA, Southern Africa, and India. [Two Sentinel-3 satellites](#)  
75 [currently flying provide revisit times of less than two days for OLCI and less than one day for the SLSTR instrument at equator.](#)  
[Swath width of the OLCI instrument is 1270 km. SLSTR swath width is 1420 km for the nadir view and 750 km for the oblique](#)  
[view.](#)

The post-process correction is based on a feed forward neural network that was trained to predict the bias in Sentinel-3  
Synergy AOD. Sentinel-3-AERONET-collocated data was used as the training data for the neural network and the trained  
80 neural network was then used for bias correction and superresolution of the Sentinel-3 AOD (land) data. The idea for post-  
process correction of satellite AOD retrievals was introduced in Lipponen et al. (2021). For the technical details and accuracy  
metrics of Sentinel-3 SYNERGY land POPCORN AOD, and related openly available code and data, see Lipponen et al. (2022).

In this work, we use POPCORN AODs at 440, 500, 550, 675, and 870 nm, and the Angstrom exponent derived using  
AODs at these wavelengths as inputs for the AOD-to-PM<sub>2.5</sub> ratio model. POPCORN AODs are the data that bring the accurate  
85 AERONET AOD information to the AOD-to-PM<sub>2.5</sub> conversion.

### 2.2 OpenAQ

OpenAQ (<https://openaq.org/>) is an open database for air quality data. In this work, we use OpenAQ as our data source for  
surface in-situ PM<sub>2.5</sub> observations. OpenAQ provides pointwise air quality measurement data for thousands of stations. The  
temporal resolution of the data provided varies by station, 1-hour and daily observations are commonly available. See Figure 1  
90 for a map of OpenAQ stations providing hourly data in our region of interest.

Some OpenAQ stations report 24 hour average  $PM_{2.5}$  every hour.

In this work, we used the 24 hour averages given every hour to estimate hourly  $PM_{2.5}$ . This was done station-by-station using a Tikhonov regularized (with regularization parameter value 0.05) least-squares fit to unfold the time integrated data into hourly estimates.

95 In practice, the hourly  $PM_{2.5}$  estimates were computed using the formula

$$\underline{PM_{2.5,1h}} = (A^T A + \alpha I)^{-1} A^T b, \quad (1)$$

where

$$A = \begin{bmatrix} \frac{1}{24} & \frac{1}{24} & \cdots & \frac{1}{24} & 0 & 0 & \cdots & 0 \\ 0 & \frac{1}{24} & \cdots & \frac{1}{24} & \frac{1}{24} & 0 & \cdots & 0 \\ & & & \vdots & & & & \\ 0 & 0 & \cdots & 0 & 0 & 0 & \cdots & \frac{1}{24} \end{bmatrix}, \quad (2)$$

$$100 \quad b = \begin{bmatrix} PM_{2.5,24h,1} \\ PM_{2.5,24h,2} \\ \vdots \\ PM_{2.5,24h,N} \end{bmatrix}, \quad (3)$$

$$\underline{PM_{2.5,1h}} = \begin{bmatrix} PM_{2.5,1h,24} \\ PM_{2.5,1h,25} \\ \vdots \\ PM_{2.5,1h,N} \end{bmatrix}, \quad (4)$$

and  $\alpha$  is the regularization parameter.  $PM_{2.5,1h,N}$  and  $PM_{2.5,24h,N}$  denote the 1 hour and 24 hour average  $PM_{2.5}$  at timestep  $N$ , respectively.

### 105 **2.3 MERRA-2**

The Modern-Era Retrospective analysis for Research and Applications, Version 2 (MERRA-2) is NASA's reanalysis model (Randles et al., 2017). MERRA-2 provides us meteorological variables, such as wind fields and temperatures. Furthermore, MERRA-2 reanalysis also has the necessary aerosol and air quality information to compute an estimate for the surface  $PM_{2.5}$ .

MERRA-2 has a spatial resolution of  $0.5^\circ \times 0.625^\circ$ . This is roughly 50 km in Central Europe region. The time-varying  
 110 MERRA-2 variables we use have the temporal resolution of 1 hour and both instantaneous values or time-averaged values are

given depending on the variable and data product. We also use some MERRA-2 constant variables as inputs for our AOD-to-PM<sub>2.5</sub> model. See the Appendix A for a list of all variables we have used as inputs in our models from the MERRA-2 re-analysis.

In addition to MERRA-2 provided variables, the following variables are derived using the MERRA-2 meteorology and aerosol-related variables and used in our models as inputs:

- **Relative humidity (RH) at the surface.** [Equation based on the Clausius-Clapeyron equation \(see e.g. Michaelides et al., 2019\)](#)

:

$$RH = 0.263 \cdot PS \cdot QLML / \exp((17.67 \cdot (T2M - 273.15)) / (T2M - 29.65))$$

- **Wind direction (WD10M) at 10 meters:**

$$WD10M = \arctan(-V10M/U10M)$$

- **Wind speed (WS10M) at 10 meters:**

$$WS10M = \sqrt{U10M^2 + V10M^2}$$

- **PM<sub>2.5</sub> at surface:** (Buchard et al. (2016))

$$PM_{2.5} = (1.375 \cdot SO4SMASS + 1.4 \cdot OCSMASS + BCSMASS + DUSMASS25 + SSSMASS25) \cdot 10^9$$

- **AOD-to-PM<sub>2.5</sub> ratio  $\eta$ :**

$$\eta = \frac{PM_{2.5}}{TOTEXTTAU}$$

## 2.4 CALIOP aerosol vertical profile climatology

We use the Cloud-Aerosol Lidar and Infrared Pathfinder Satellite Observation (CALIPSO) Lidar Level-3 Tropospheric Aerosol Profiles, Cloud Free Data, Standard Version 4-20 data product as one of our input data source (NASA, 2022; Winker et al., 2010). This level-3 climatology data product has spatial resolution of 2.5 deg x 2 deg and temporal resolution of 1 month. We use daytime variables and in the case of missing data, we use the nearest value found in the dataset. We use two variables from this dataset: AOD 63 Percent Below and AOD 90 Percent Below. These variables indicate the vertical height below which 63 and 90 percent of AOD is located on average. This gives us information about the vertical distribution of aerosols in the atmosphere.

## 2.5 Time variables

Information about the time of day and year are given as inputs for the model. Both the yearly and daily fractions from the beginning of the year and day until the end of year and day, respectively, are mapped to a unit circle and the x and y coordinates of the unit circle points are used as inputs for the model. With this approach, we get very similar values for the end and beginning of the year and day.

## 140 2.6 High-resolution geographical indicators

### 2.6.1 OpenStreetMap roads

OpenStreetMap is an open map project and it contains map data with high spatial resolution. We use OpenStreetMap roads as a data source for our model inputs. We compute the distance to the nearest street or highway and use this distance as an input. [We use a 100 meter resolution grid for the distances.](#) The paths, streets and highways are all classified as 'highways' in  
145 OpenStreetMap and we use only the following sub-classes to only accept roads and highways with car traffic and thus potential PM<sub>2.5</sub> sources (information from (OpenStreetMap, 2023)). See Appendix A for all the OpenStreetMap road types used to compute the distance to the closest road.

### 2.6.2 NASA Black Marble Night Lights

NASA's Black Marble is a night light product based on Visible Infrared Imaging Radiometer Suite (VIIRS) day/night band  
150 (DNB) radiances measured at nighttime. DNB is highly sensitive to light and can therefore detect even very low intensity lights on Earth surface at night. Most of the nighttime lights seen on Earth's surface are due to human activities. As human footprint is well seen in the night lights, we use the NASA Black Marble Night Lights as a proxy variable for the population density and use it as one input for our models. [We use Night Light data at spatial resolution of 500 meter as our input based on the yearly data product VNP46A4 \(Wang et al., 2020\).](#)

### 155 2.6.3 MODIS land cover type

We use MODIS MCD12Q1 (Sulla-Menashe and Friedl, 2018) land cover type data product to derive input variables that contain distances to the closest International Geosphere Biosphere Programme (IGBP) land cover types (Loveland and Belward, 1997; Belward et al., 1999). The spatial resolution of the MODIS MCD12Q1 data product is 500 meters. For the list of IGBP land cover types, see Appendix A.

### 160 2.6.4 Digital Elevation Model

We use the Advanced Spaceborne Thermal Emission and Reflection Radiometer (ASTER) digital elevation model (DEM) to describe the land surface elevation (Fujisada et al., 2011, 2012; NASA/METI/AIST/Japan Spacesystems, and US/Japan ASTER Science Team, 2019). ASTER DEM has a spatial resolution of 1 arcsecond corresponding to about 30 meters.

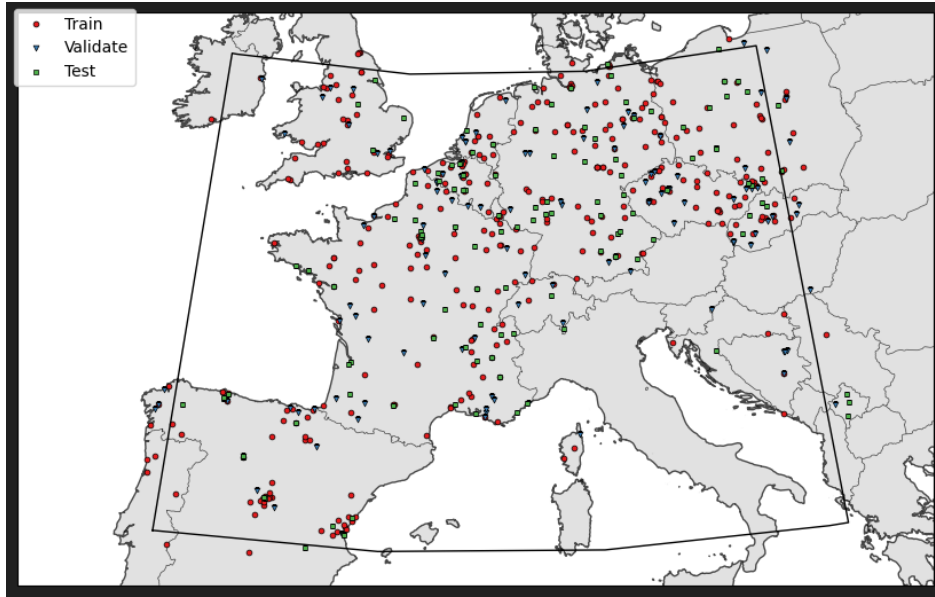


**Figure 1.** Map of stations in the region of interest.

### 3 Methods

#### 165 3.1 AOD-to-PM<sub>2.5</sub> conversion

Similarly as, for example, in van Donkelaar et al. (2021), we model the dependency between the PM<sub>2.5</sub> at the surface level and AOD using the following model

$$\underline{PM}_{2.5} = \eta \cdot \underline{AOD}, \quad (5)$$

where  $\eta = \eta(\mathbf{x}, t) = \eta(\mathbf{r}, t)$  is the AOD-to-PM<sub>2.5</sub> conversion coefficient that is function of both time and space  $\mathbf{r}$ .

#### 170 3.2 Post-process correction approach

Let  $y \in \mathbb{R}^m$  denote an accurate satellite retrieval

$$y = f(x), \quad (6)$$

where vector  $y$  contains the output of the satellite retrieval algorithm,  $f : \mathbb{R}^n \mapsto \mathbb{R}^m$  is an accurate retrieval algorithm and  $x \in \mathbb{R}^n$  contains all the algorithm inputs including the observation geometry and level 1 satellite observation data such as the top-of-atmosphere reflectances. The retrieval  $y$  can consist, for example, of surface PM<sub>2.5</sub> at a given point in space and time.

In practice, due to uncertainties in the auxiliary parameters of the underlying forward model, extensive computational dimension of the problems and processing time limitations, it is not possible to construct an accurate retrieval algorithm  $f$  but an

approximate retrieval algorithm

$$\tilde{y} \approx \tilde{f}(x) \quad (7)$$

180 has to be employed instead. The approximate retrieval  $\tilde{f}$  is typically based on physically simplified and computationally reduced approximate forward models that are used due to [the](#) huge dimensionality of the retrieval problems and the need for computational efficiency. The utilization of the approximate retrieval algorithm leads to an *approximation error*

$$e(x) = f(x) - \tilde{f}(x) \quad (8)$$

in the retrieval parameters.

185 The core idea of the *model enforced* post-process correction model is to improve the accuracy of the approximate retrieval (7) by machine learning techniques. By Equations (6)-(8), the accurate retrieval can be written as

$$\begin{aligned} y &= f(x) \\ &= \tilde{f}(x) + [f(x) - \tilde{f}(x)] \\ &= \tilde{f}(x) + e(x). \end{aligned} \quad (9)$$

190 To obtain the corrected retrieval, Equation (9) is used to combine the conventional (physics-based) retrieval algorithm  $\tilde{f}(x)$  and a machine learning based model  $\hat{e}(x)$  to predict the realization of the approximation error  $e(x)$  to obtain an corrected retrieval

$$y \approx \tilde{f}(x) + \hat{e}(x). \quad (10)$$

Note that this approach is different from a conventional *fully learned* machine learning model in which the aim is to emulate the accurate retrieval algorithm  $f(x)$  with a machine learning model

$$195 \quad y \approx \hat{f}(x) \quad (11)$$

that is trained to predict the retrieval  $y$  directly from the satellite observation and geometry data  $x$ .

### 3.3 Correction of AOD-to-PM<sub>2.5</sub> conversion factor $\eta$

In our work, we use the post-process correction approach (10) to correct for the MERRA-2-based AOD-to-PM<sub>2.5</sub> conversion factor  $\eta$ . We utilize an ensemble of neural networks to learn the correction to the conversion factor  $\eta$  and producing simultaneously error envelopes related to the learning process. Our post process correction model  ~~$\hat{e}(x)$~~   $\hat{e}(x) : \mathbb{R}^n \mapsto \mathbb{R}$  corrects the conversion factor pixel-by-pixel, meaning that

$$\hat{e}(x) : \mathbb{R}^n \mapsto \mathbb{R}.$$

$$\eta(x) \equiv \hat{\eta} + \hat{e}(x) \quad (12)$$

$$205 \quad \text{PM}_{2.5} \equiv \eta(x) \cdot \text{AOD}_{\text{POPCORN}} \quad (13)$$

where  $\hat{\eta}$  represents the AOD-to-PM<sub>2.5</sub> ratio to be corrected. The correction model is learned using collocated data from ground station PM<sub>2.5</sub>-PM<sub>2.5</sub> data, MERRA-2 data, satellite data and retrieval, meteorological data, and high-resolution geographical indicators. All the inputs used can be found in Table A1 and are described in Section 2. We used SHAP analysis (Lundberg and Lee, 2017) in order to estimate feature importance after the training of the model. In fig.A1 you can see a bar plot of the first 26 input features ordered by their importance (SHAP value) and in Table A1 the feature are ordered by their SHAP importance (from left to right and from top to bottom). Since no features showed non-negligible SHAP value, we decided to keep them all in the training of the model. We finally add the estimated correction term to the MERRA-2  $\eta$  values and calculate the PM<sub>2.5</sub> estimates corresponding to POPCORN AOD retrievals using Equation (5).

### 3.4 Selection of the network model

As the dimension  $n$  of the input data  $x$  to the correction model  $\hat{e}(x)$  is relatively small ( $n = 172$ ) and output is a scalar, we utilize a fully connected feedforward neural network for the regression task. The networks are implemented using the TensorFlow framework.

To optimize the neural network architecture, we employed KerasTuner, a hyperparameter optimization framework. The Adam optimizer and  $10^{-3}$  learning rate were selected. We used the Mean Square Error (MSE) loss function in the training. Linear-A linear activation function was employed for the output layer as the correction  $\hat{e}(x)$  is real valued. Other parameters, such as the activation functions and the number of nodes in hidden layers, were optimized using KerasTuner. We considered the number of hidden layers, experimenting with 2, 3, and 4-layer architectures. The model with two hidden layers led to slightly better accuracy compared to the deeper models with 3 or 4 hidden layers and thus we employed the architecture with two hidden layers as our final model. The final optimal neural network architecture comprises of 172 input features and two hidden layers with seLu activation functions. The first and second hidden layers consisted of 160 and 128 neurons, respectively. Figure 2 shows the neural network architecture obtained from the model optimization.

We divided the dataset into three subsets in training our neural network model. Specifically, 60% of the data was used for training, 20% for validation, and 20% for testing, see Figure 1 for the division of the AQ stations into the training, validation and test sites. The learning data was divided into training, validation and test data by stations instead of random division of data points in order to avoid model overfitting and having test data from locations within the region of interest that were not included in the model training. Figure 3 shows the proportions of different PM<sub>2.5</sub> values in the train, validate and test data. We used the validation set and the early stopping technique with the patience of 30 to avoid overfitting of the neural network model.

In our tests, the model struggled to predict high PM<sub>2.5</sub> values accurately. We partially attributed this limitation to the skewed distribution of our dataset, which was predominantly composed of low PM<sub>2.5</sub> values, see Figure 3 for the histogram of the PM<sub>2.5</sub> values of the AQ stations in the learning data. To address this, we introduced a cut-off value of  $80 \mu\text{g m}^{-3}$  for PM<sub>2.5</sub> and trained our model with samples corresponding to PM<sub>2.5</sub> values only below this. Furthermore, we experimented with reweighting the loss function to emphasize higher PM<sub>2.5</sub> values. Although this strategy slightly improved the model's performance on

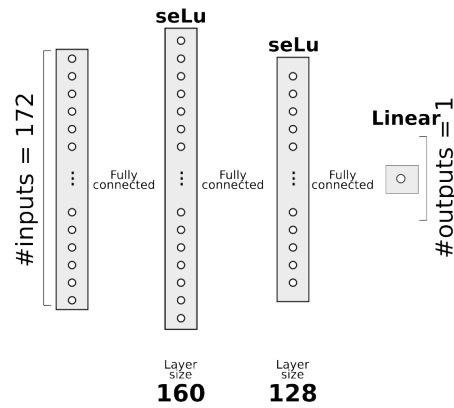


**Figure 2.** Feed-forward neural network architecture for post-process correction of  $\eta$  ratio, optimized with KerasTuner. The model contains two hidden layers with seLu activation functions (160 and 128 nodes respectively) and a single node output layer with linear activation function.

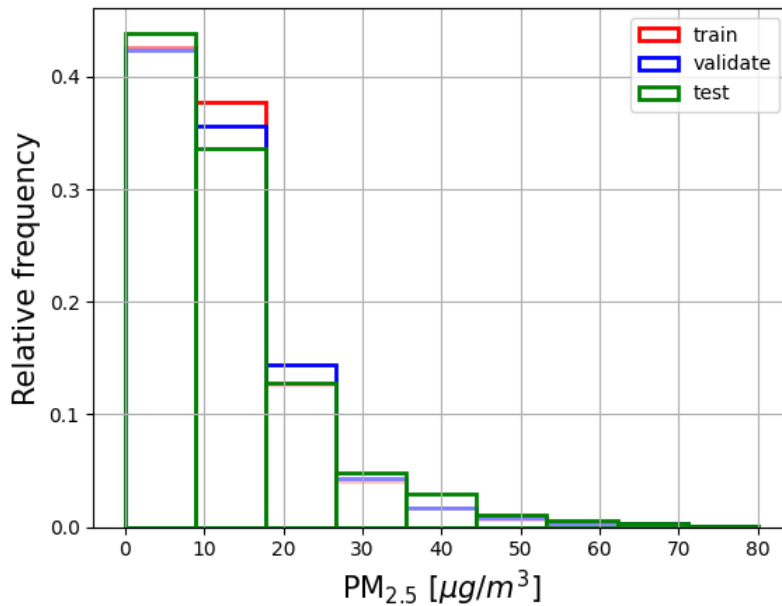


**Figure 3.** Distribution of AQ station  $PM_{2.5}$  values in training, validation, and test sets. The training data is used to train the machine learning algorithm, while the validation data is used to prevent overfitting. The test data is used to test the results after training. The division of the data was obtained by dividing the AQ stations in the region of interest to three separate sets with 60%, 20% and 20% shares of training, validation and test stations.



the high-end tail, it compromised the accuracy on the low-end tail. Consequently, we decided not to use the reweighted loss  
240 function.

### 3.5 Ensemble of networks

To address the problem of local minima and dependency on the initialization in neural network training we used an ensemble  
based technique where we trained an ensemble of 80 networks each initialized with different random weights. We considered  
the predictions of the networks as samples from a distribution and used the median of the predictions as a point estimate for  
245 the correction term of  $\eta$ . We use the spread minimum to maximum interval of the 80 outputs of the networks as an learning  
related uncertainty for  $\eta$  which was propagated onward to uncertainty of the  $\text{PM}_{2.5}$  estimates through the conversion (5).

## 4 Results

Figure 4 shows scatter plots of the satellite and model-based predictions of  $\text{PM}_{2.5}$  with respect to the values of the ground stations  
for the test data AQ stations per single-overpass and as monthly averages. We calculated the monthly averages considering a  
250 threshold: monthly averages were accepted only when we had more than 5 daily measurements per month (and station). The  
figures on the top row show results for single-overpasses and the figures on the bottom row show monthly averages. The figures  
on the left show the ground data ~~comparison-comparison~~ for the MERRA-2  $\text{PM}_{2.5}$  estimates, the figures on the middle show the  
ground data ~~comparison-comparison~~ for the  $\text{PM}_{2.5}$  values estimated using Equation (5) with POPCORN AOD and MERRA-  
2 conversion factor  $\eta$ , and the figures on the right show the ~~comparison-comparison~~ for the  $\text{PM}_{2.5}$  values estimated using  
255 Equation (5) with POPCORN AOD and post-process corrected  $\eta$ . As can be seen, the use of post-process corrected conversion  
factor leads to a clear improvement on the accuracy of the predictions of  $\text{PM}_{2.5}$  at the independent test data locations. The  $R^2$   
coefficient ~~per single-overpass for instantaneous values~~ is improved by about ~~270%-290%~~ compared to both the MERRA-2  
prediction and the estimate (5) with POPCORN AOD and MERRA-2 conversion factor; ~~the RMSE of~~. The RMSE is improved  
by a factor 32% compared to MERRA-2 prediction and of by a factor 41% compared to the product of POPCORN AOD with  
260 MERRA-2  $\eta$ ; and the. The absolute value of the bias is reduced by a factor over 99%-95% respect to both of the uncorrected  
estimates, and the MAE decreased by a factor 26% compared to MERRA-2 prediction and by a factor 41% compared to the  
product of POPCORN AOD with MERRA-2  $\eta$ . In the monthly averages the  $R^2$  coefficient is improved by a factor ~~600%~~  
~~350%~~ respect to MERRA-2 prediction and by a factor ~~250%-279%~~ compared to the estimate (5) with POPCORN AOD and  
MERRA-2  $\eta$ . The RMSE in the monthly averages is reduced by a factor ~~43%-over 47%~~ with respect to both uncorrected  
265 methods. The bias in the monthly averages is reduced by a factor ~~83% and 76%, respectively~~ ~~92% and 89%, respectively, and~~  
the MAE decreased by a factor 44% and 49%.

We remark that we tested also the fully-learned approach (11) for learning directly the AOD-to- $\text{PM}_{2.5}$  conversion factor  $\eta$   
values instead of the correction of the MERRA-2 based conversion, but the results with the fully learned approach were less  
accurate than with the post-correction approach (10).

270 Figures 5 and 6 show  $PM_{2.5}$  maps over Paris (23 February 2019) and Madrid (29 March 2019) for a single satellite overpass, respectively. On the top-left the uncorrected map is obtained based on POPCORN AOD ~~550nm~~-500nm and MERRA-2  $\eta$ , while on the top-right the corrected map uses the post-process corrected MERRA-2  $\eta$ . On the bottom left we compare the satellite based  $PM_{2.5}$  values to the measured  $PM_{2.5}$  values at the AQ stations which are represented by the circles in the maps. The red circles represent the post-corrected estimates (medians calculated from the ensemble predictions), the black dots the uncorrected estimates while the blue dots the ground based measurement values at the stations. The red error bars represent the spread of  $PM_{2.5}$  values coming from the ensemble of networks and they are to be considered as uncertainty estimates related to the machine learning process. The joint RMSE of the uncorrected estimates with respect to the ground stations are ~~8.26~~ 7.82  $\mu g/m^3$  and ~~5.17~~ 4.59  $\mu g/m^3$  respectively for Paris and Madrid, and the joint RMSE for the post-corrected estimates with respect the ground stations are ~~7.86~~ 6.36  $\mu g/m^3$  and ~~4.93~~ 2.27  $\mu g/m^3$ , indicating improved accuracy of the per overpass  $PM_{2.5}$  estimates in the post process correction approach. The figure reveals that, for all the stations, the different initialization points for the trainings improve over the uncorrected prediction. The median of the ensemble predictions is not always better than the uncorrected prediction, but the uncertainty interval is either enclosing the measured value or is closer to the measured value than the uncorrected estimate. The bottom right images show a time series of  $PM_{2.5}$  monthly averages predictions against the time series coming from a ground station monthly averages (the stations are pointed on the corrected maps by a white arrow). The red envelopes show the uncertainty envelope of the post-process corrected estimate. Here the ground station monthly averages are contained in the uncertainty envelope. Figure 7 shows time series of  $PM_{2.5}$  monthly averages of the post-process corrected estimates for different stations in the region of interest, showing good alignment with the accurate ground based AQ measurements. Similar performance was found out for the monthly averages in most of the test stations in the region of interest, indicating that the post process corrected estimates of monthly averages of  $PM_{2.5}$  are generally well aligned with the accurate ground based observations.

295 The post process correction method we have proposed here is flexible with respect data to be utilized in the training, as it allows straightforward addition of more training data (by re-optimization of the neural network architecture) coming from different data sources in order to improve the  $PM_{2.5}$  predictions. In this study, we demonstrated the approach using POPCORN AOD data, which is obtained post-correcting Sentinel-3 AOD. The approach can also be extended and trained to other satellite instruments and their AOD products to obtain similarly post-process corrected high-resolution satellite estimates of  $PM_{2.5}$ , leading to more frequent temporal sampling of a particular location. In this study, we demonstrated the approach using a relatively large region-of-interest covering central Europe year 2019. The approach can also be scaled in a straightforward manner to smaller or larger regions of interest by changing the training data.

## 5 Conclusions

300 We developed an innovative machine learning technique aimed at correcting the AOD-to- $PM_{2.5}$  ratio derived from MERRA-2 data. This correction method integrates data from various sources, including ground station  $PM_{2.5}$  data, MERRA-2 data, satellite data, meteorological data, and high-resolution geographical indicators. The post process corrected AOD-to- $PM$  ratio

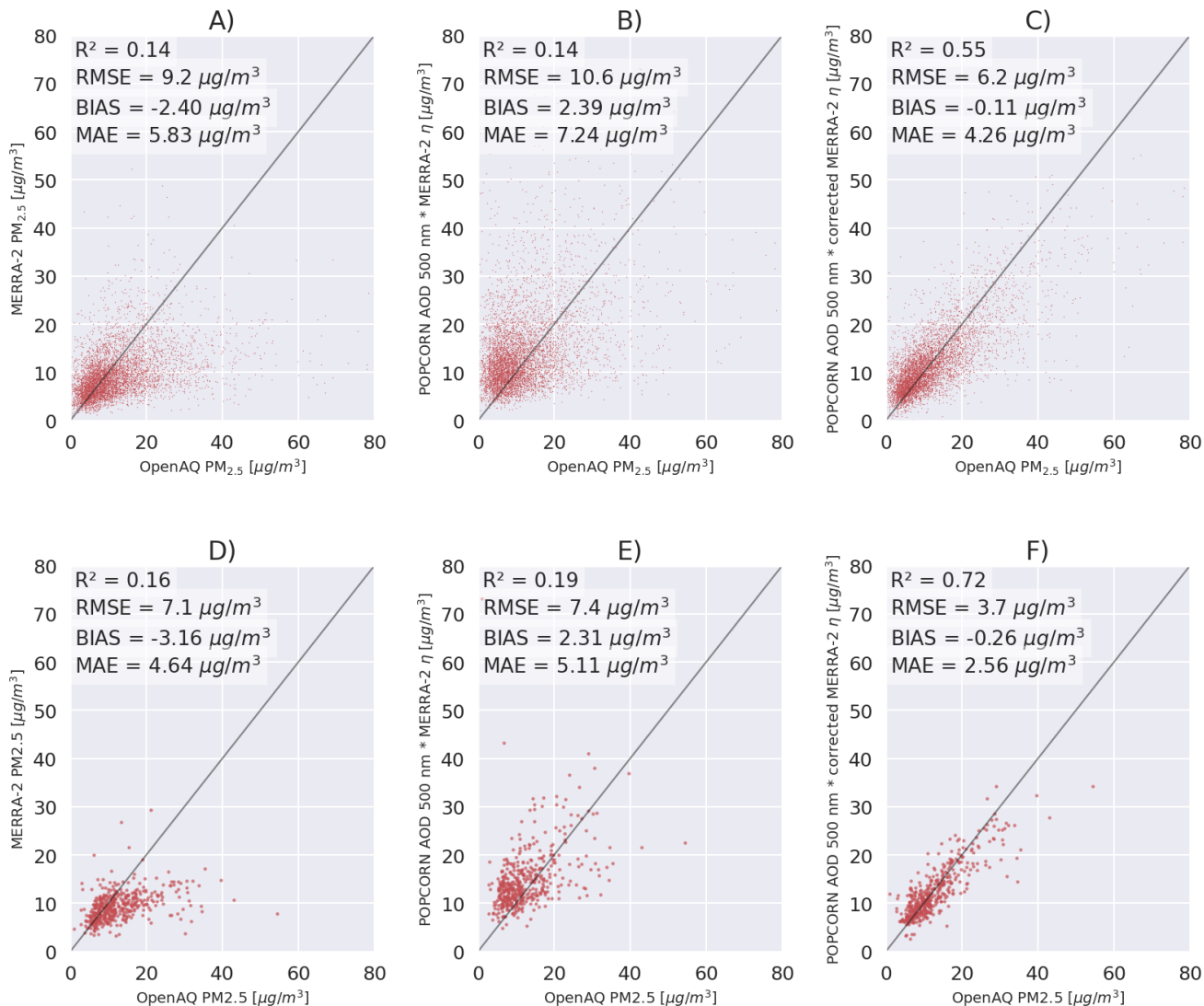


**Figure 4.** A) MERRA-2 PM<sub>2.5</sub> predictions against OpenAQ PM<sub>2.5</sub> measurements per single-overpass. B) Uncorrected NOODLESALAD PM<sub>2.5</sub> predictions against OpenAQ PM<sub>2.5</sub> measurements per single-overpass. C) Corrected NOODLESALAD PM<sub>2.5</sub> predictions against OpenAQ PM<sub>2.5</sub> measurements per single-overpass. D) MERRA-2 monthly averages PM<sub>2.5</sub> predictions against OpenAQ monthly averages PM<sub>2.5</sub> measurements. E) Uncorrected NOODLESALAD monthly averages PM<sub>2.5</sub> predictions against OpenAQ monthly averages PM<sub>2.5</sub> measurements. F) Corrected NOODLESALAD monthly averages PM<sub>2.5</sub> predictions against OpenAQ monthly averages PM<sub>2.5</sub> measurements.

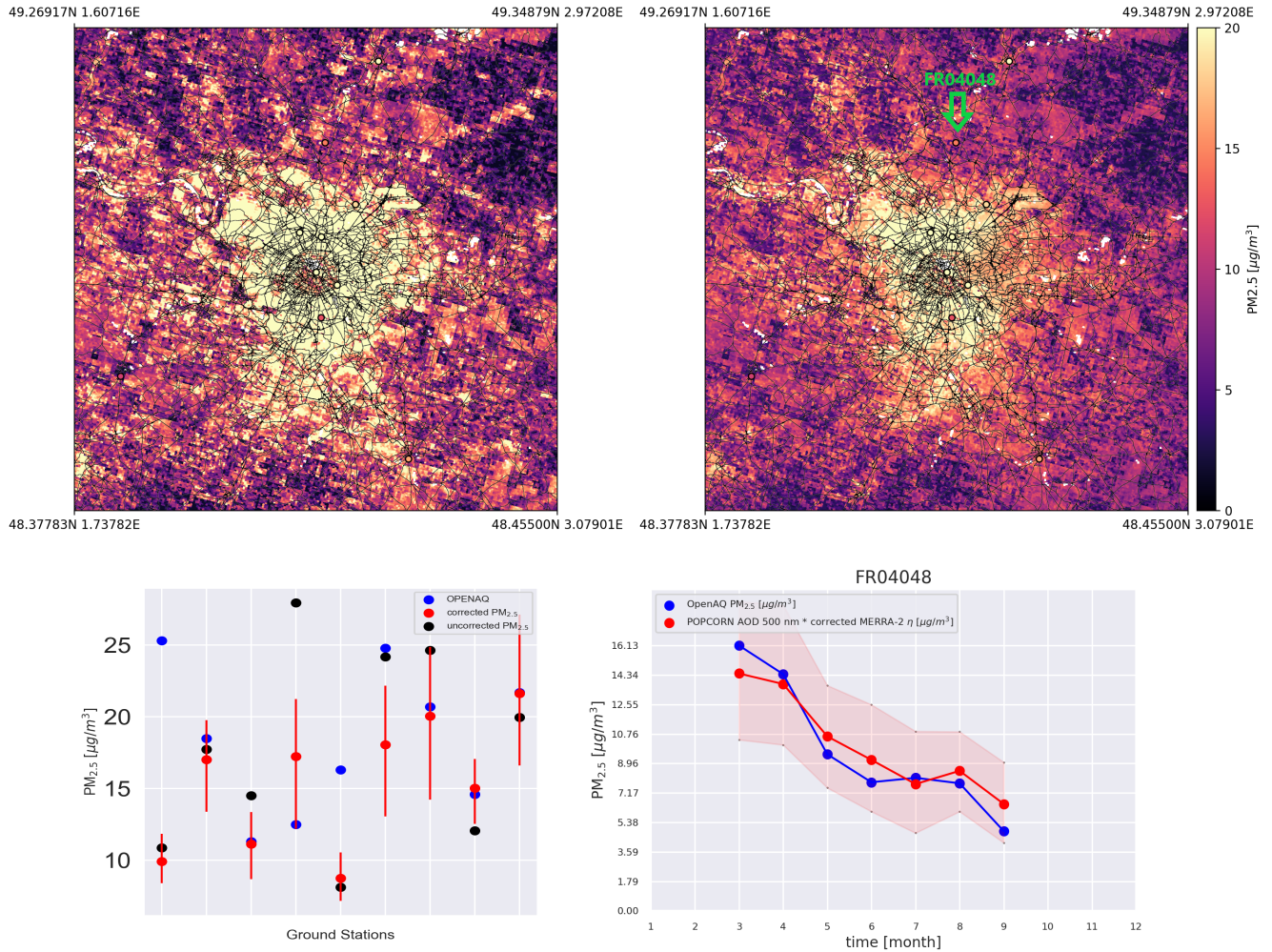


**Figure 5.** On the top-left: single overpass not-corrected PM<sub>2.5</sub> map over Paris (RMSE against ground stations = ~~8.26~~7.82 μg/m<sup>3</sup>). On the top-right: single overpass corrected PM<sub>2.5</sub> map over Paris (RMSE against ground stations = ~~7.86~~6.36 μg/m<sup>3</sup>). Notice that the white regions for the figures on top are regions where the AOD (so the PM<sub>2.5</sub>) values are missing because of cloud contamination. On the bottom-left: comparison of the uncorrected and corrected method at the ground stations, The red error bars represent the spread of values obtained through the ensemble method, while the red dots represent the medians of those values. On the bottom-right: comparison between OpenAQ and corrected method predicted time series of PM<sub>2.5</sub> monthly averages at a single station (indicated on the corrected map by a ~~white~~green arrow). The red envelope represents the uncertainty coming from the ensemble method.



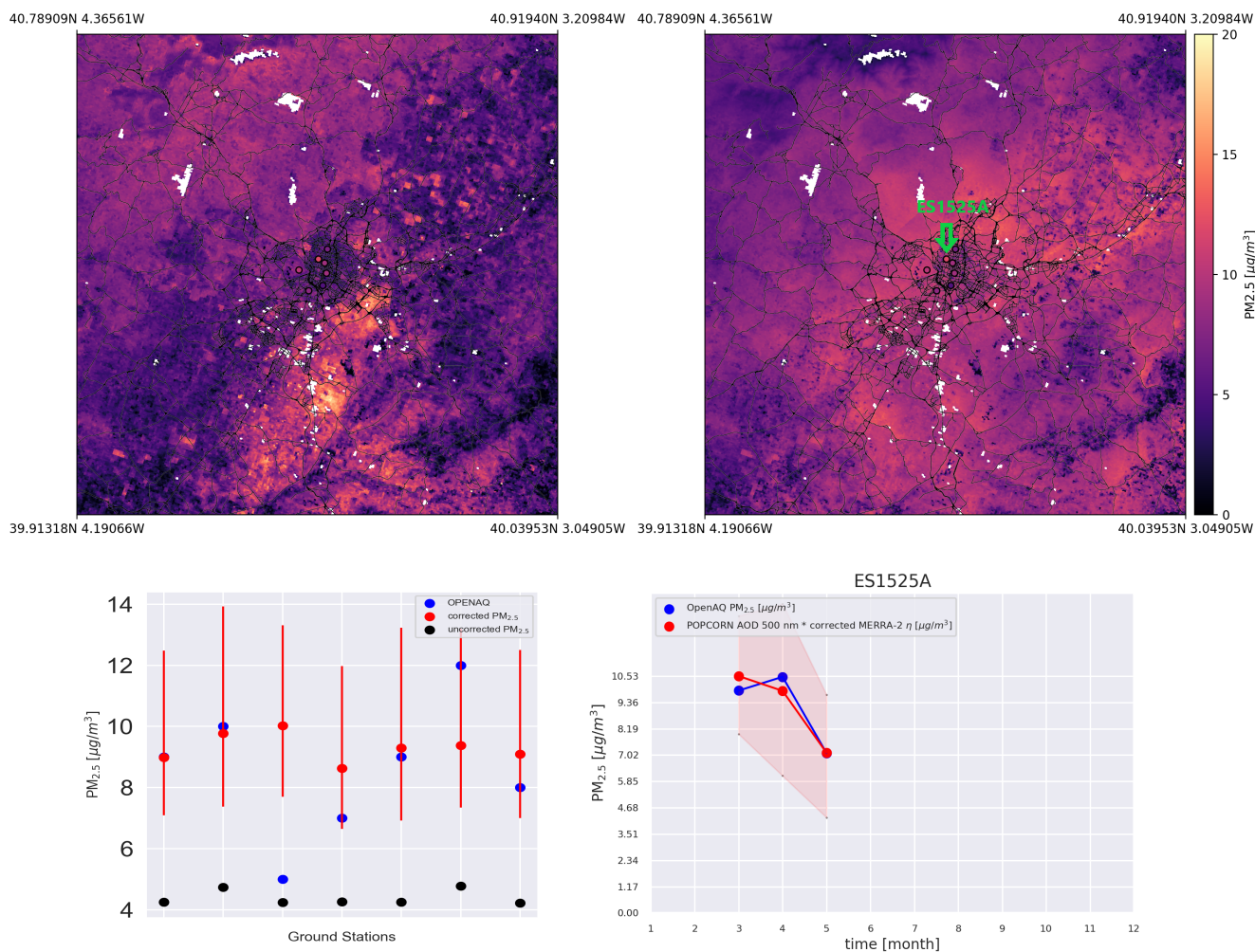


**Figure 6.** On the top-left: single overpass not-corrected PM<sub>2.5</sub> map over Madrid (RMSE against ground stations = ~~5.17~~ 4.59 μg/m<sup>3</sup>). On the top-right: single overpass corrected PM<sub>2.5</sub> map over Madrid (RMSE against ground stations = ~~1.93~~ 2.27 μg/m<sup>3</sup>). Notice that the white regions for the figures on top are regions where the AOD (so the PM<sub>2.5</sub>) values are missing because of cloud contamination. On the bottom-left: comparison of the uncorrected and corrected method at the ground stations. The red error bars represent the spread of values obtained through the ensemble method, while the red dots represent the medians of those values. On the bottom-right: comparison between OpenAQ and corrected method predicted time series of PM<sub>2.5</sub> monthly averages at a single station (indicated on the corrected map by a ~~white~~ green arrow). The red envelope represents the uncertainty coming from the ensemble method.

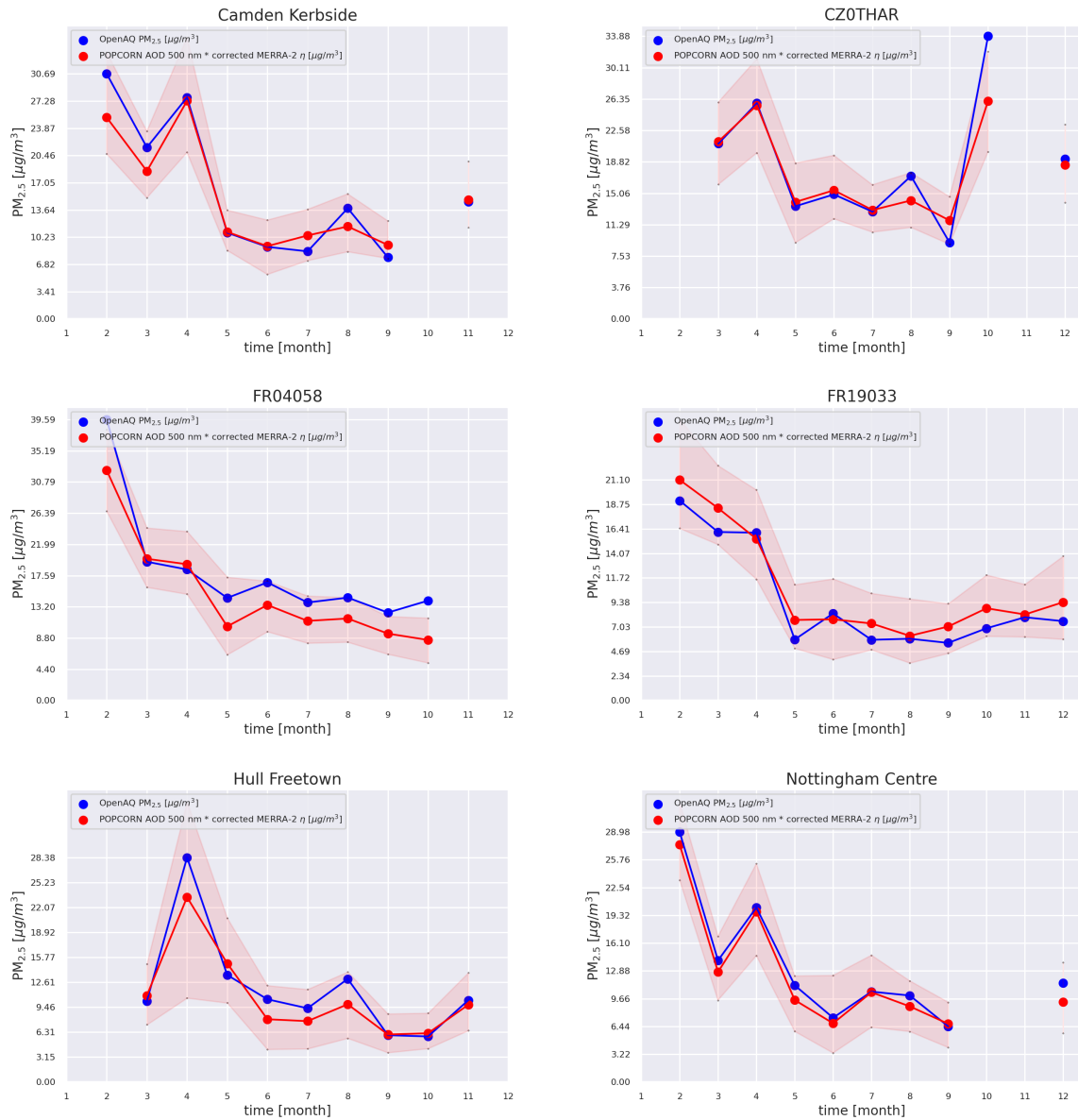


**Figure 7.** Monthly averages time series for six stations from the independent test set within the region of interest. The red envelopes represent the uncertainty coming from the ensemble method.

was then employed to estimate  $PM_{2.5}$  levels within the Central Europe region for the year 2019. Our approach outperforms MERRA-2 predictions and predictions made using MERRA-2 AOD-to-PM ratio and POPCORN AOD, resulting in improvement in all evaluated metrics, whether considering individual overpasses or monthly averages. The  $PM_{2.5}$  estimates were derived by aggregating the median values from an ensemble of neural networks. We incorporated the ensemble's value spread as a measure of machine learning related uncertainty in the post-process corrected  $PM_{2.5}$  estimates, and our estimates with their uncertainty envelopes were found to be generally highly feasible with respect the accurate ground based observations at the independent test station locations. We remark that while our approach produced generally good accuracy in estimation of  $PM_{2.5}$ , it exhibited poorer performance for the high end values of  $PM_{2.5}$ . This finding can be attributed to small number of learning data for the high end tail of  $PM_{2.5}$  values in our region of interest, highlighting the obvious fact that the learning data for machine learning needs to be representative for the operational environment and conditions.

In this study, our goal was to utilize a simple neural network model to estimate the  $PM_{2.5}$  values from satellite data. Therefore, the adoption of a fully connected neural network architecture was considered a reasonable choice. The architecture of the network was determined through a combination of manual selection and the use of KerasTuner to optimize the number of neurons per layer and the activation function. This ensured the development of an effective network for the specific problem under study. The robust performance of the resulting model highlights the efficacy of employing a simple neural network model to address  $PM_{2.5}$  estimation with notable success.

*Code and data availability.* Sentinel-3 Synergy Land POPCORN dataset is openly available for download at [https://a3s.fi/swift/v1/AUTH\\_ca5072b7b22e463b85a2739fd6cd5732/POPCORNdata/readme.html](https://a3s.fi/swift/v1/AUTH_ca5072b7b22e463b85a2739fd6cd5732/POPCORNdata/readme.html). The OpenAQ data is open data and available for download at <https://openaq.org/>. The OpenStreetMap data is open data and available for download at <https://www.openstreetmap.org/>. All the NASA data (MERRA-2, CALIOP, MODIS, ASTER DEM) used in this work is open data and can be found and downloaded using the NASA Earthdata Search website at <https://www.earthdata.nasa.gov/>. The NASA Black Marble Night Lights data is available at <https://blackmarble.gsfc.nasa.gov/>. Code will be available from the authors on a reasonable request.

*Author contributions.* **Andrea Porcheddu:** Conceptualization, Methodology, Software, Formal analysis, Writing — Original draft, Visualization **Ville Kolehmainen:** Conceptualization, Methodology, Formal analysis, Writing — Original draft, Supervision **Timo Lähivaara:** Conceptualization, Methodology, Formal analysis, Writing - Original Draft, Supervision **Antti Lipponen:** Conceptualization, Methodology, Software, Formal analysis, Writing — Original draft, Visualization, Supervision

*Competing interests.* The authors declare no competing interests.

330 *Acknowledgements.* This study was funded by the European Space Agency EO Science for Society programme via the NOODLESALAD project (contract number 4000137651/22/I-DT-Ir). The research was also supported by the ~~Academy of Finland, the~~ Finnish Centre of Excellence of Inverse Modelling and Imaging (project no. ~~336791~~)~~and the Academy-353084~~, [Flagship of Advanced Mathematics for Sensing Imaging and Modelling \(grant no. 358944\)](#), and the [Research Council](#) of Finland (project no. 321761). The authors wish to acknowledge CSC – IT Center for Science, Finland, for computational resources.



## 335 Appendix A: Lists of variables used from datasets

### A1 MERRA-2 variables

We use the following meteorology-related variables from the MERRA-2 M2T1NXSLV dataset:

- **PS**: surface pressure (Pa)
- **QV10M**: 10-meter specific humidity ( $\text{kg kg}^{-1}$ )
- 340 – **QV2M**: 2-meter specific humidity ( $\text{kg kg}^{-1}$ )
- **SLP**: sea level pressure (Pa)
- **T10M**: 10-meter air temperature (K)
- **T2M**: 2-meter air temperature (K)
- **TO3**: total column ozone (Dobsons)
- 345 – **TOX**: total column odd oxygen ( $\text{kg m}^{-2}$ )
- **TQI**: total precipitable ice water ( $\text{kg m}^{-2}$ )
- **TQL**: total precipitable liquid water ( $\text{kg m}^{-2}$ )
- **TQV**: total precipitable water vapor ( $\text{kg m}^{-2}$ )
- **TROPPB**: tropopause pressure based on blended estimate (Pa)
- 350 – **TROPPT**: tropopause pressure based on thermal estimate (Pa)
- **TROPPV**: tropopause pressure based on EPV estimate (Pa)
- **TROPQ**: tropopause specific humidity using blended TROPP estimate ( $\text{kg kg}^{-1}$ )
- **TROPT**: tropopause temperature using blended TROPP estimate (K)
- **TS**: surface skin temperature (K)
- 355 – **U10M**: 10-meter eastward wind (m / s)
- **U2M**: 2-meter eastward wind (m / s)
- **U50M**: eastward wind at 50 meters (m / s)
- **V10M**: 10-meter northward wind (m / s)

– **V2M**: 2-meter northward wind (m / s)

360 – **V50M**: northward wind at 50 meters (m / s)

We use the following meteorology-related variables from the MERRA-2 M2T1NXFLX dataset:

– **BSTAR**: surface bouyancy scale ( $\text{m s}^{-2}$ )

– **CDH**: surface exchange coefficient for heat ( $\text{kg m}^{-2} \text{s}^{-1}$ )

– **CDM**: surface exchange coefficient for momentum ( $\text{kg m}^{-2} \text{s}^{-1}$ )

365 – **CDQ**: surface exchange coefficient for moisture ( $\text{kg m}^{-2} \text{s}^{-1}$ )

– **CN**: surface neutral drag coefficient (1)

– **DISPH**: zero plane displacement height (m)

– **EFLUX**: total latent energy flux ( $\text{W m}^{-2}$ )

– **EVAP**: evaporation from turbulence ( $\text{kg m}^{-2} \text{s}^{-1}$ )

370 – **FRCAN**: areal fraction of anvil showers (1)

– **FRCCN**: areal fraction of convective showers (1)

– **FRCLS**: areal fraction of nonanvil large scale showers (1)

– **FRSEAIICE**: ice covered fraction of tile (1)

– **GHTSKIN**: ground heating for skin temp ( $\text{W m}^{-2}$ )

375 – **HFLUX**: sensible heat flux from turbulence ( $\text{W m}^{-2}$ )

– **HLML**: surface layer height (m)

– **NIRDF**: surface downwelling nearinfrared diffuse flux ( $\text{W m}^{-2}$ )

– **NIRDR**: surface downwelling nearinfrared beam flux ( $\text{W m}^{-2}$ )

– **PBLH**: planetary boundary layer height (m)

380 – **PGENTOT**: total column production of precipitation ( $\text{kg m}^{-2} \text{s}^{-1}$ )

– **PRECANV**: anvil precipitation ( $\text{kg m}^{-2} \text{s}^{-1}$ )

– **PRECCON**: convective precipitation ( $\text{kg m}^{-2} \text{s}^{-1}$ )

- **PRECLSC**: nonanvil large scale precipitation ( $\text{kg m}^{-2} \text{s}^{-1}$ )
- **PRECSNO**: snowfall ( $\text{kg m}^{-2} \text{s}^{-1}$ )
- 385 – **PRECTOT**: total precipitation from atm model physics ( $\text{kg m}^{-2} \text{s}^{-1}$ )
- **PRECTOTCORR**: Bias corrected total precipitation ( $\text{kg m}^{-2} \text{s}^{-1}$ )
- **PREVTOT**: total column re-evap/subl of precipitation ( $\text{kg m}^{-2} \text{s}^{-1}$ )
- **QLML**: surface specific humidity (1)
- **QSH**: effective surface specific humidity ( $\text{kg kg}^{-1}$ )
- 390 – **QSTAR**: surface moisture scale ( $\text{kg kg}^{-1}$ )
- **RHOA**: air density at surface ( $\text{kg m}^{-3}$ )
- **RISFC**: surface bulk Richardson number (1)
- **SPEED**: surface wind speed ( $\text{m s}^{-1}$ )
- **SPEEDMAX**: surface wind speed ( $\text{m s}^{-1}$ )
- 395 – **TAUGWX**: surface eastward gravity wave stress ( $\text{N m}^{-2}$ )
- **TAUGWY**: surface northward gravity wave stress ( $\text{N m}^{-2}$ )
- **TAUX**: eastward surface stress ( $\text{N m}^{-2}$ )
- **TAUY**: northward surface stress ( $\text{N m}^{-2}$ )
- **TCZPBL**: transcom planetary boundary layer height (m)
- 400 – **TLML**: surface air temperature (K)
- **TSH**: effective surface skin temperature (K)
- **TSTAR**: surface temperature scale (K)
- **ULML**: surface eastward wind ( $\text{m s}^{-1}$ )
- **USTAR**: surface velocity scale ( $\text{m s}^{-1}$ )
- 405 – **VLML**: surface northward wind ( $\text{m s}^{-1}$ )
- **Z0H**: surface roughness for heat (m)

- **Z0M**: surface roughness (m)

We use the following aerosol and air quality related variables from the MERRA-2 M2T1NXAER dataset:

- **BCANGSTR**: Black Carbon Angstrom parameter [470-870 nm] (1)
- 410 – **BCCMASS**: Black Carbon Column Mass Density ( $\text{kg m}^{-2}$ )
- **BCEXTTAU**: Black Carbon Extinction AOT [550 nm] (1)
- **BCFLUXU**: Black Carbon column u-wind mass flux ( $\text{kg m}^{-1} \text{s}^{-1}$ )
- **BCFLUXV**: Black Carbon column v-wind mass flux ( $\text{kg m}^{-1} \text{s}^{-1}$ )
- **BCSCATAU**: Black Carbon Scattering AOT [550 nm] (1)
- 415 – **BCSMASS**: Black Carbon Surface Mass Concentration ( $\text{kg m}^{-3}$ )
- **DMSCMASS**: DMS Column Mass Density ( $\text{kg m}^{-2}$ )
- **DMSSMASS**: DMS Surface Mass Concentration ( $\text{kg m}^{-3}$ )
- **DUANGSTR**: Dust Angstrom parameter [470-870 nm] (1)
- **DUCMASS**: Dust Column Mass Density ( $\text{kg m}^{-2}$ )
- 420 – **DUCMASS25**: Dust Column Mass Density - PM 2.5 ( $\text{kg m}^{-2}$ )
- **DUEXTT25**: Dust Extinction AOT [550 nm] - PM 2.5 (1)
- **DUEXTTAU**: Dust Extinction AOT [550 nm] (1)
- **DUFLUXU**: Dust column u-wind mass flux ( $\text{kg m}^{-1} \text{s}^{-1}$ )
- **DUFLUXV**: Dust column v-wind mass flux ( $\text{kg m}^{-1} \text{s}^{-1}$ )
- 425 – **DUSCAT25**: Dust Scattering AOT [550 nm] - PM 2.5 (1)
- **DUSCATAU**: Dust Scattering AOT [550 nm] (1)
- **DUSMASS**: Dust Surface Mass Concentration ( $\text{kg m}^{-3}$ )
- **DUSMASS25**: Dust Surface Mass Concentration - PM 2.5 ( $\text{kg m}^{-3}$ )
- **OCANGSTR**: Organic Carbon Angstrom parameter [470-870 nm] (1)
- 430 – **OCCMASS**: Organic Carbon Column Mass Density ( $\text{kg m}^{-2}$ )

- **OCEXTTAU**: Organic Carbon Extinction AOT [550 nm] (1)
- **OCFLUXU**: Organic Carbon column u-wind mass flux ( $\text{kg m}^{-1} \text{s}^{-1}$ )
- **OCFLUXV**: Organic Carbon column v-wind mass flux ( $\text{kg m}^{-1} \text{s}^{-1}$ )
- **OCSCATAU**: Organic Carbon Scattering AOT [550 nm] (1)
- 435 – **OCSMASS**: Organic Carbon Surface Mass Concentration ( $\text{kg m}^{-3}$ )
- **SO2CMASS**: SO2 Column Mass Density ( $\text{kg m}^{-2}$ )
- **SO2SMASS**: SO2 Surface Mass Concentration ( $\text{kg m}^{-3}$ )
- **SO4CMASS**: SO4 Column Mass Density ( $\text{kg m}^{-2}$ )
- **SO4SMASS**: SO4 Surface Mass Concentration ( $\text{kg m}^{-3}$ )
- 440 – **SSANGSTR**: Sea Salt Angstrom parameter [470-870 nm] (1)
- **SSCMASS**: Sea Salt Column Mass Density ( $\text{kg m}^{-2}$ )
- **SSCMASS25**: Sea Salt Column Mass Density - PM 2.5 ( $\text{kg m}^{-2}$ )
- **SSEXTT25**: Sea Salt Extinction AOT [550 nm] - PM 2.5 (1)
- **SSEXTTAU**: Sea Salt Extinction AOT [550 nm] (1)
- 445 – **SSFLUXU**: Sea Salt column u-wind mass flux ( $\text{kg m}^{-1} \text{s}^{-1}$ )
- **SSFLUXV**: Sea Salt column v-wind mass flux ( $\text{kg m}^{-1} \text{s}^{-1}$ )
- **SSSCAT25**: Sea Salt Scattering AOT [550 nm] - PM 2.5 (1)
- **SSSCATAU**: Sea Salt Scattering AOT [550 nm] (1)
- **SSSMASS**: Sea Salt Surface Mass Concentration ( $\text{kg m}^{-3}$ )
- 450 – **SSSMASS25**: Sea Salt Surface Mass Concentration - PM 2.5 ( $\text{kg m}^{-3}$ )
- **SUANGSTR**: SO4 Angstrom parameter [470-870 nm] (1)
- **SUEXTTAU**: SO4 Extinction AOT [550 nm] (1)
- **SUFLUXU**: SO4 column u-wind mass flux ( $\text{kg m}^{-1} \text{s}^{-1}$ )
- **SUFLUXV**: SO4 column v-wind mass flux ( $\text{kg m}^{-1} \text{s}^{-1}$ )

- 455 – **SUSCATAU**: SO4 Scattering AOT [550 nm] (1)
- **TOTANGSTR**: Total Aerosol Angstrom parameter [470-870 nm] (1)
- **TOTEXTTAU**: Total Aerosol Extinction AOT [550 nm] (1)
- **TOTSCATAU**: Total Aerosol Scattering AOT [550 nm] (1)

## A2 OpenStreetMap road types used to compute the distance to the closest road

460 We use the following road types to compute the distance to the closest road. The descriptions of the road types are obtained from OpenStreetMap (2023).

- **motorway**: A restricted access major divided highway, normally with 2 or more running lanes plus emergency hard shoulder. Equivalent to the Freeway, Autobahn, etc.
- **trunk**: The most important roads in a country's system that aren't motorways.
- 465 – **primary**: The next most important roads in a country's system.
- **secondary**: The next most important roads in a country's system.
- **tertiary**: The next most important roads in a country's system.
- **motorway\_link**: The link roads (sliproads/ramps) leading to/from a motorway from/to a motorway or lower class highway. Normally with the same motorway restrictions.
- 470 – **trunk\_link**: The link roads (sliproads/ramps) leading to/from a trunk road from/to a trunk road or lower class highway.
- **primary\_link**: The link roads (sliproads/ramps) leading to/from a primary road from/to a primary road or lower class highway.
- **secondary\_link**: The link roads (sliproads/ramps) leading to/from a secondary road from/to a secondary road or lower class highway.
- 475 – **tertiary\_link**: The link roads (sliproads/ramps) leading to/from a tertiary road from/to a tertiary road or lower class highway.

## A3 IGBP land cover types

IGBP classification contains the following land cover types:

- **1**: Evergreen needleleaf forests
- 480 – **2**: Evergreen broadleaf forests

- 3: Deciduous needleleaf forests
- 4: Deciduous broadleaf forests
- 5: Mixed forests
- 6: Closed shrublands
- 485 – 7: Open shrublands
- 8: Woody savannas
- 9: Savannas
- 10: Grasslands
- 11: Permanent wetlands
- 490 – 12: Croplands
- 13: Urban and built-up
- 14: Cropland/natural
- 15: Snow and ice
- 16: Barren
- 495 – 17: Water bodies

**A4 Table of all input variables**

MERRA2_POPCORN_ELEVATIONDIFFERENCE	POPCORN_AOD500	POPCORN_AOD870
MERRA2_ETA	MERRA2_FLX_GHTSKIN	POPCORN_distancetolandclass2
POPCORN_time_cyclic_yearly_sin	POPCORN_time_cyclic_yearly_cos	POPCORN_AOD675
MERRA2_surface_to_column_ratio_PM25	POPCORN_AOD550	MERRA2_ASMCONST_SGH
POPCORN_distancetolandclass6	MERRA2_AER_BCFLUXU	MERRA2_AER_SO2CMASS
MERRA2_ASM_QV2M	POPCORN_ANGSTROM	MERRA2_AER_DUSMASS
MERRA2_AER_SSSMASS25	POPCORN_AOD440	MERRA2_ASM_TROPT
MERRA2_AER_TOTANGSTR	MERRA2_ASM_QV10M	MERRA2_ASM_T2M
MERRA2_AER_OCCMASS	MERRA2_ASM_TQV	MERRA2_FLX_QLML
MERRA2_AER_SUFLUXV	MERRA2_FLX_USTAR	MERRA2_AER_SO4CMASS
POPCORN_distancetolandclass17	MERRA2_AER_DUCMASS	MERRA2_AER_BCSMASS
MERRA2_AER_BCSCATAU	MERRA2_AER_DUEXTTAU	MERRA2_FLX_EFLUX
MERRA2_AER_SO4SMASS	MERRA2_FLX_EVAP	MERRA2_FLX_NIRDR
MERRA2_FLX_HFLUX	POPCORN_ASTERDEM	MERRA2_AER_SUANGSTR
MERRA2_ASM_TROPPB	MERRA2_AER_BCFLUXV	MERRA2_FLX_TLML
MERRA2_FLX_QSTAR	POPCORN_time_cyclic_daily_sin	MERRA2_AER_DUSCATAU
MERRA2_FLX_PBLH	POPCORN_distancetolandclass7	POPCORN_distancetolandclass12
MERRA2_AER_OCSCATAU	MERRA2_AER_TOTEXTTAU	POPCORN_distancetolandclass15
MERRA2_ASM_TROPPV	MERRA2_SURFACERH	MERRA2_FLX_RHOA
MERRA2_AER_BCEXTTAU	MERRA2_FLX_FRCLS	MERRA2_AER_DUEXTT25
MERRA2_ASM_T10M	MERRA2_ASM_TS	MERRA2_FLX_SPEED
MERRA2_AER_BCANGSTR	MERRA2_AER_DUSCAT25	MERRA2_AER_OCFLUXU
MERRA2_CTMCONST_FRLANDICE	MERRA2_AER_DUCMASS25	MERRA2_AER_OCEXTTAU
MERRA2_FLX_FRCAN	MERRA2_ASMCONST_FRLAND	MERRA2_AER_SSCMASS
MERRA2_AER_TOTSCATAU	MERRA2_AER_BCCMASS	MERRA2_CTMCONST_FRACI
MERRA2_AER_DUSMASS25	POPCORN_distancetolandclass16	POPCORN_CALIOP_MASK_AOD_90_Percent_Below
POPCORN_time_cyclic_daily_cos	POPCORN_distancetolandclass4	MERRA2_AER_DUANGSTR
MERRA2_FLX_SPEEDMAX	MERRA2_CTMCONST_FRLAND	MERRA2_FLX_HLML
MERRA2_AER_DUFLUXV	MERRA2_AER_OCANGSTR	MERRA2_FLX_TAU
MERRA2_FLX_FRCCN	MERRA2_PM25	MERRA2_ASMCONST_FRLAKE
POPCORN_distancetolandclass8	MERRA2_AER_SSFLUXV	MERRA2_AER_SUFLUXU
MERRA2_FLX_CDQ	POPCORN_distancetolandclass13	MERRA2_FLX_TSTAR
MERRA2_FLX_CN	MERRA2_ASM_V50M	MERRA2_AER_SSSCATAU
MERRA2_FLX_QSH	MERRA2_FLX_Z0H	MERRA2_ASM_PS
MERRA2_AER_SSEXTTAU	MERRA2_FLX_TCZPBL	MERRA2_AER_OCSMASS
MERRA2_FLX_TSH	POPCORN_distancetolandclass3	MERRA2_SURFACEELEVATION
MERRA2_ASM_TROPQ	MERRA2_FLX_CDH	MERRA2_FLX_PGENTOT
MERRA2_ASM_U10M	MERRA2_FLX_ULML	MERRA2_ASM_TOX
MERRA2_AER_DMSCMASS	POPCORN_distancetolandclass1	POPCORN_distancetolandclass14
MERRA2_FLX_TAU	MERRA2_ASMCONST_FRLANDICE	MERRA2_AER_SUSCATAU
MERRA2_AER_DUFLUXU	POPCORN_distancetolandclass10	MERRA2_FLX_PREVTOT
MERRA2_CTMCONST_FROCEAN	MERRA2_ASM_TQL	MERRA2_ASM_U2M
MERRA2_ASM_DISP	MERRA2_FLX_PRECTOT	MERRA2_AER_SO2SMASS
MERRA2_FLX_CDM	MERRA2_FLX_Z0M	MERRA2_ASM_windspeed
POPCORN_distancetolandclass11	MERRA2_FLX_DISP	MERRA2_AER_OCFLUXV
MERRA2_FLX_PRECTOTCORR	MERRA2_ASM_TROPPT	MERRA2_FLX_PRECLSC
MERRA2_FLX_BSTAR	MERRA2_ASM_TO3	POPCORN_CALIOP_MASK_AOD_63_Percent_Below
MERRA2_FLX_PRECCON	MERRA2_ASM_TQI	MERRA2_ASMCONST_FROCEAN
MERRA2_CTMCONST_PHIS	POPCORN_distancetolandclass5	MERRA2_CTMCONST_FRLAKE
MERRA2_FLX_TAUWX	MERRA2_FLX_PRECANV	MERRA2_ASM_V2M
MERRA2_ASMCONST_PHIS	MERRA2_FLX_NIRDF	POPCORN_distancetolandclass9
MERRA2_ASM_SLP	POPCORN_BlackMarble	POPCORN_distancetoroad_upwind
MERRA2_AER_SSANGSTR	MERRA2_FLX_VLML	MERRA2_AER_SSSCAT25
MERRA2_ASM_windirection	MERRA2_FLX_TAUWY	MERRA2_AER_SSFLUXU
MERRA2_AER_SUEXTTAU	MERRA2_ASM_V10M	MERRA2_AER_SSCMASS25
MERRA2_FLX_PRECSNO	MERRA2_AER_SSEXTT25	MERRA2_AER_DMSSMASS
MERRA2_FLX_RISFC	MERRA2_AER_SSSMASS	MERRA2_ASM_U50M
MERRA2_FLX_FRSEAICE		

**Table A1.** List of input variables used in our model ordered by SHAP value (from left to right and from top to bottom).



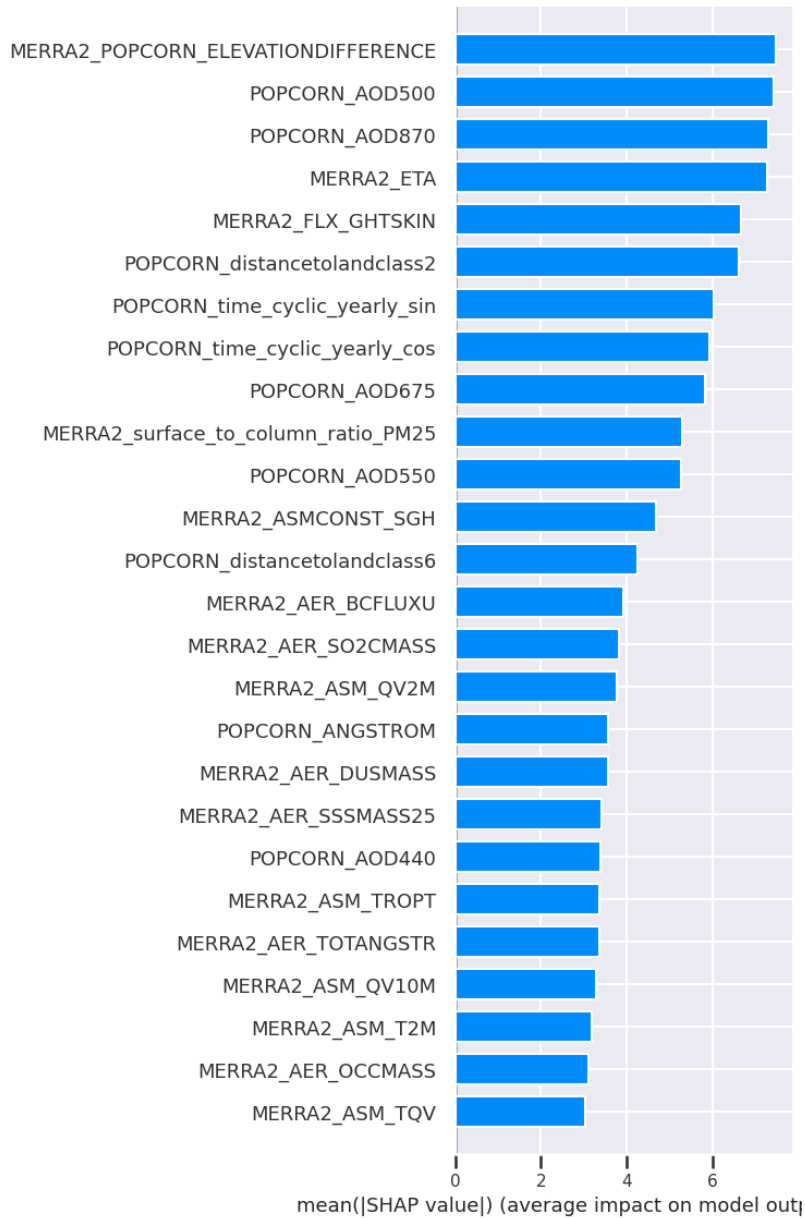


**Figure A1.** [Bar plot of the SHAP values for the first 26 input variables in order of importance.](#)

## References

Belward, A. S., Estes, J. E., and Kline, K. D.: The IGBP-DIS global 1-km land-cover data set DISCover: A project overview, *Photogrammetric Engineering and Remote Sensing*, 65, 1013–1020, 1999.

- 500 Buchard, V., Da Silva, A., Randles, C., Colarco, P., Ferrare, R., Hair, J., Hostetler, C., Tackett, J., and Winker, D.: Evaluation of the surface PM<sub>2.5</sub> in Version 1 of the NASA MERRA Aerosol Reanalysis over the United States, *Atmospheric Environment*, 125, 100–111, 2016.
- Cohen, A. J., Brauer, M., Burnett, R., Anderson, H. R., Frostad, J., Estep, K., et al.: Estimates and 25-year trends of the global burden of disease attributable to ambient air pollution: an analysis of data from the Global Burden of Diseases Study 2015, *The Lancet*, 389, 1907–1918, 2017.
- 505 Fujisada, H., Urai, M., and Iwasaki, A.: Advanced methodology for ASTER DEM generation, *IEEE transactions on geoscience and remote sensing*, 49, 5080–5091, 2011.
- Fujisada, H., Urai, M., and Iwasaki, A.: Technical methodology for ASTER global DEM, *IEEE Transactions on Geoscience and Remote Sensing*, 50, 3725–3736, 2012.
- Geng, G., Zhang, Q., Martin, R., Donkelaar, A., Huo, H., CHE, H., Lin, J., and He, H.: Estimating long-term PM<sub>2.5</sub> concentrations in China using satellite-based aerosol optical depth and a chemical transport model, *Remote Sensing of Environment*, 166, <https://doi.org/10.1016/j.rse.2015.05.016>, 2015.
- 510 Hammer, M. S., van Donkelaar, A., Li, C., Lyapustin, A., Sayer, A. M., Hsu, N. C., Levy, R. C., Garay, M. J., Kalashnikova, O. V., Kahn, R. A., et al.: Global estimates and long-term trends of fine particulate matter concentrations (1998–2018), *Environmental Science & Technology*, 54, 7879–7890, 2020.
- 515 Handschuh, J., Erbertseder, T., and Baier, F.: Systematic Evaluation of Four Satellite AOD Datasets for Estimating PM<sub>2.5</sub> Using a Random Forest Approach, *Remote Sensing*, 15, <https://doi.org/10.3390/rs15082064>, 2023.
- Health Effects Institute: State of global air 2019, 2019.
- Ibrahim, S., Landa, M., Pešek, O., Brodský, L., and Halounová, L.: Machine Learning-Based Approach Using Open Data to Estimate PM<sub>2.5</sub> over Europe, *Remote Sensing*, 14, <https://doi.org/10.3390/rs14143392>, 2022.
- 520 Lipponen, A., Kolehmainen, V., Kolmonen, P., Kukkurainen, A., Mielonen, T., Sabater, N., Sogacheva, L., Virtanen, T. H., and Arola, A.: Model-enforced post-process correction of satellite aerosol retrievals, *Atmospheric Measurement Techniques*, 14, 2981–2992, 2021.
- Lipponen, A., Reinval, J., Väisänen, A., Taskinen, H., Lähivaara, T., Sogacheva, L., Kolmonen, P., Lehtinen, K., Arola, A., and Kolehmainen, V.: Deep-learning-based post-process correction of the aerosol parameters in the high-resolution Sentinel-3 Level-2 Synergy product, *Atmospheric Measurement Techniques*, 15, 895–914, 2022.
- 525 Loveland, T. R. and Belward, A.: The international geosphere biosphere programme data and information system global land cover data set (DISCover), *Acta Astronautica*, 41, 681–689, 1997.
- Lundberg, S. M. and Lee, S.: A unified approach to interpreting model predictions, *CoRR*, [abs/1705.07874](https://arxiv.org/abs/1705.07874), <http://arxiv.org/abs/1705.07874>, 2017.
- Michaelides, S., Lane, J., and Kasparis, T.: Effect of Vertical Air Motion on Disdrometer Derived Z-R Coefficients, *Atmosphere*, 10, 77, 530 2019.
- NASA: CALIPSO Data User’s Guide, [https://www-calipso.larc.nasa.gov/resources/calipso\\_users\\_guide/](https://www-calipso.larc.nasa.gov/resources/calipso_users_guide/), [Online; accessed 13-April-2023], 2022.
- NASA/METI/AIST/Japan Spacesystems, and US/Japan ASTER Science Team: ASTER Global Digital Elevation Model V003, distributed by NASA EOSDIS Land Processes DAAC, 2019.
- 535 OpenStreetMap: OpenStreetMap Wiki - Key:highway, <https://wiki.openstreetmap.org/wiki/Key:highway>, [Online; accessed 13-April-2023], 2023.

- Pope, C. A. I. and Dockery, D. W.: Health Effects of Fine Particulate Air Pollution: Lines that Connect, *Journal of the Air & Waste Management Association*, 56, 709–742, <https://doi.org/10.1080/10473289.2006.10464485>, 2006.
- 540 Randles, C., Da Silva, A., Buchard, V., Colarco, P., Darmenov, A., Govindaraju, R., Smirnov, A., Holben, B., Ferrare, R., Hair, J., et al.: The MERRA-2 aerosol reanalysis, 1980 onward. Part I: System description and data assimilation evaluation, *Journal of climate*, 30, 6823–6850, 2017.
- Schneider, R., Vicedo-Cabrera, A. M., Sera, F., Masselot, P., Stafoggia, M., de Hoogh, K., Kloog, I., Reis, S., Vieno, M., and Gasparrini, A.: A Satellite-Based Spatio-Temporal Machine Learning Model to Reconstruct Daily PM<sub>2.5</sub> Concentrations across Great Britain, *Remote Sensing*, 12, <https://doi.org/10.3390/rs12223803>, 2020.
- 545 Stafoggia, M., Bellander, T., Bucci, S., Davoli, M., de Hoogh, K., de' Donato, F., Gariazzo, C., Lyapustin, A., Michelozzi, P., Renzi, M., Scortichini, M., Shtein, A., Viegli, G., Kloog, I., and Schwartz, J.: Estimation of daily PM<sub>10</sub> and PM<sub>2.5</sub> concentrations in Italy, 2013–2015, using a spatiotemporal land-use random-forest model, *Environment International*, 124, 170–179, <https://doi.org/https://doi.org/10.1016/j.envint.2019.01.016>, 2019.
- Sulla-Menashe, D. and Friedl, M. A.: User guide to collection 6 MODIS land cover (MCD12Q1 and MCD12C1) product, USGS: Reston, VA, USA, 1, 18, 2018.
- 550 Taskinen, H., Väisänen, A., Hatakka, L., Virtanen, T. H., Lähivaara, T., Arola, A., Kolehmainen, V., and Lipponen, A.: High-Resolution Post-Process Corrected Satellite AOD, *Geophysical Research Letters*, 49, e2022GL099733, 2022.
- van Donkelaar, A., Martin, R. V., Spurr, R. J., Drury, E., Remer, L. A., Levy, R. C., and Wang, J.: Optimal estimation for global ground-level fine particulate matter concentrations, *Journal of Geophysical Research: Atmospheres*, 118, 5621–5636, 2013.
- 555 van Donkelaar, A., Martin, R. V., Brauer, M., Hsu, N. C., Kahn, R. A., Levy, R. C., Lyapustin, A., Sayer, A. M., and Winker, D. M.: Global Estimates of Fine Particulate Matter using a Combined Geophysical-Statistical Method with Information from Satellites, Models, and Monitors, *Environmental Science & Technology*, 50, 3762–3772, <https://doi.org/10.1021/acs.est.5b05833>, 2016.
- van Donkelaar, A., Hammer, M. S., Bindle, L., Brauer, M., Brook, J. R., Garay, M. J., Hsu, N. C., Kalashnikova, O. V., Kahn, R. A., Lee, C., Levy, R. C., Lyapustin, A., Sayer, A. M., and Martin, R. V.: Monthly Global Estimates of Fine Particulate Matter and Their Uncertainty, *Environmental Science & Technology*, 55, 15287–15300, <https://doi.org/10.1021/acs.est.1c05309>, 2021.
- 560 Wang, Z., Shrestha, R., and M.O., R.: VIIRS/NPP Lunar BRDF-Adjusted Nighttime Lights Yearly L3 Global 15 arc second Linear Lat Lon Grid [data set], <https://doi.org/10.5067/VIIRS/VNP46A4.001>, 2020.
- Winker, D., Pelon, J., Coakley Jr, J., Ackerman, S., Charlson, R., Colarco, P., Flamant, P., Fu, Q., Hoff, R., Kittaka, C., et al.: The CALIPSO mission: A global 3D view of aerosols and clouds, *Bulletin of the American Meteorological Society*, 91, 1211–1230, 2010.
- 565 World Health Organization: New WHO Global Air Quality Guidelines aim to save millions of lives from air pollution, <https://www.who.int/news/item/22-09-2021-new-who-global-air-quality-guidelines-aim-to-save-millions-of-lives-from-air-pollution>, [Online; accessed 12-April-2023], 2021.
- Zhang, H. and Kondragunta, S.: Daily and Hourly Surface PM<sub>2.5</sub> Estimation From Satellite AOD, *Earth and Space Science*, 8, e2020EA001599, <https://doi.org/https://doi.org/10.1029/2020EA001599>, e2020EA001599 2020EA001599, 2021.